

# Parallel Adaptive Anisotropic Meshing on cc-NUMA Machines

Christos Tsolakis and Nikos Chrisochoides

CRTC, Department of Computer Science, Old Dominion  
University, Norfolk, VA, USA.

## Abstract

Efficient and robust anisotropic mesh adaptation is crucial for Computational Fluid Dynamics (CFD) simulations. The CFD Vision 2030 Study highlights the pressing need for this technology, particularly for simulations targeting supercomputers. This work applies a fine-grained speculative approach to anisotropic mesh operations. Our implementation exhibits more than 90% parallel efficiency on a multi-core node. Additionally, we evaluate our method within an adaptive pipeline for a spectrum of publicly available test-cases that includes both analytically derived and error-based fields. For all test-cases, our results are in accordance with published results in the literature. Support for CAD-based data is introduced, and its effectiveness is demonstrated on one of NASA's High-Lift prediction workshop cases.

## 1 Introduction

The goal of mesh adaptation is to modify an existing mesh so that it can accurately capture features of the underlying simulation. Metric-based methods guide the process of mesh adaptation through the use of metric fields. Metric fields control the orientation and size of the elements individually **for each** direction, thus enabling the creation of anisotropic meshes. Metric-based methods have been utilized in a breadth of applications, including solving neutron transfer problems in nuclear physics [1], efficiently applying diffusion tensor calculus on medical imaging data [2] and topology optimization in structural mechanics [3]. In the CFD field, metric-based methods are capable of resolving both inviscid [4] and viscous flows over complex geometries [5].

The CFD 2030 Vision [6] study identifies efficient and robust mesh adaptation as one of the key areas that need improvement to advance CFD simulations. In [7], the authors present an overview of mesh adaptation and offer suggestions for achieving the objectives outlined in the CFD Vision study. One of the recommendations is to optimize existing adaptive techniques to function effectively on current and future systems. An example of these architectures is *Frontier*, the world's first public exascale machine [8] that can provide the platform for simulation analyses at high fidelity. As of today *Frontier* is composed out of 74 cabinets, each cabinet holds 64 blades, and each blade has two 64-core nodes for a total of 60,6208 CPU cores.

Handling these kind of hardware efficiently starts by using an efficient shared memory implementation of mesh adaptation operations. *CDT3D* is a *scalability-first* approach to mesh adaptation that implements a scalable software an initially incomplete functionality and the intention of completing functionality as it is needed.

*CDT3D* uses the speculative method that explores concurrency at a fine-grain (element) level by executing in parallel multiple meshing kernels that attempt to capture their dependencies upon runtime. If any of the kernels fail to capture its dependencies, due to conflicts with another kernel, it will release its acquired dependencies and proceed to a different element.

In previous work [9] we compared an earlier version of the method of this paper against state-of-the-art anisotropic mesh adaptation methods from both the industry and academia that included both *scalability-* and *functionality-first* approaches. The analysis of the paper shows that *CDT3D* provides comparable mesh quality to the other methods for the cases studied in the paper.

In this work, we describe the implementation of the speculative fine-grained scheme for anisotropic mesh generation and adaptivity of *CDT3D* in detail and evaluate the generated meshes in a number of CFD applications. In particular, the contributions of this work include:

- Application of the speculative fine-grained scheme to a family of metric-aware mesh operations applicable to volume and boundary adaptation (Section 3). As seen in previous work [9] this combination is highly effective. As of today and to the best of the authors knowledge, it offers on shared memory machines the highest strong scaling speedup among *scalability-first* approaches and better weak scaling speedup than state-of-the-art *functionality-first* approaches. This is achieved via the low startup cost of our methods and the nature of the optimistic/speculative approach that exploits parallelism as soon as possible. Moreover, the ability to adapt both surface and volume elements at the same time yields better robustness and offers more than 3 orders of magnitude improvement when compared to adapting only the volume.
- Extension of the above operations in order to support for geometrical (CAD-based) models (Section 4). Access to a geometrical kernel allows to

interrogate the underlying domain and recover information about its curvature and local feature size which could be absent in a coarse mesh representation which is often the starting point of the adaptation procedure. Handling of CAD data gives access to well-known verification examples like the ONERA-M6 wing and the JAXA highlift model.

- Evaluation of the method in an adaptive pipeline that includes a CFD solver and real-world geometry cases and comparison of the computed quantities with values present in the literature (Section 5). In contrast to our previous work that focused mainly on element quality measures, we compiled a suite of publicly available cases and bring our attention to the main goal of mesh adaptation: capturing features of the underlying simulation. At the same time, we test how well *CDT3D* operates as a part of an adaptive pipeline composed of open-source components.

In the next couple of sections, we review related methods in the literature (Section 2). Appendix A provides a short introduction on the use of metric spaces for mesh adaptation.

## 2 Related work

The method presented in this work belongs to the wider class of *Tightly Coupled* methods for parallel mesh generation [10, 11]. Tightly Coupled methods are characterized by intense communication. Communication can be direct through messages or indirect through accessing regions of shared memory which due to false sharing and cache invalidation creates overheads. Moreover, synchronization primitives and constructs such as locks and barriers add to the overall overhead.

One of the first speculative tightly coupled methods for mesh generation is presented in [12, 13]. This method is designed for distributed-memory architectures and it uses the Delaunay kernel [14, 15] for introducing new points into the mesh. The main idea is to allow multiple cavity expansions (i.e. dependency resolutions) to take place in parallel, however, in this approach, the data dependencies are evaluated and acquired at run-time and not in any pre-processing step. This characteristic gives this method the name *speculative* or *optimistic*. If the dependency acquisition is successful the operation is applied otherwise, the process “rollbacks” to the previous state by releasing any acquired data dependencies. Although the amount of rollbacks is low, the intense communication incurs many messages, resulting in sub-optimal results. Still, by acting directly upon touched data, this approach improves cache utilization and allows tolerating more than 80% of system latencies [13]. Later efforts extend this approach to a tightly-coupled Parallel Delaunay Triangulation algorithm in [16] and an image-to-mesh method [17, 18] optimized for Distributed Shared Memory machines (DSM).

A more complete review of parallel mesh generation methods categorized by communication intensity appears in [11]. Due to length constraints, we limit our review section to parallel metric-based mesh adaptation methods instead

of parallel mesh generation methods in general. All the presented methods utilize a mix of the same elementary mesh operations: Point Insertion for refining larger than the target elements, edge collapse for suppressing small edges and elements attached to them, Edge-Face swapping for improving the quality of small clusters through topological operations as well as Vertex Smoothing to improve the quality of the elements attached to a vertex. There are, however significant differences in the implementation of each operation across the various mesh adaptation approaches/strategies which we present below. Adopting the characterization of methods followed in [11], we organize the related work into two categories based on the workload decomposition method.

Data decomposition methods decompose the data that corresponds to the given domain into datasets that can be safely accessed and updated. This category includes *Pragmatic* as presented in [19, 20] and *Omega\_h* [21]. Both methods are based on coloring the dependency graph of the cavities of their mesh operations in order to exploit parallelism. Once coloring is in place the methods evaluate the quality of the elements in a cavity before and after applying the mesh operation. The optimal configuration between the two is then picked and the mesh is updated. *Pragmatic* defers the connectivity updates until the end of the mesh iteration to allow for updating the data structure in parallel. *Omega\_h* on the other hand is based on data structures designed specifically for mesh adaptation [22] and offers a unique approach where during each adaptation pass the mesh becomes read-only and a new updated copy is derived.

Another method based on data decomposition is described in [23, 24]. This method deals with parallelism by creating mesh-specific data structures [25] designed to handle concurrent read and write access in a distributed memory environment resembling distributed databases. Moreover, it has been extended for metric-based adaptation in [26]. Each mesh operator pass is coupled with a global synchronization step where all the processes commit and receive modifications of the boundary elements.

Domain decomposition methods decompose the initial mesh into subdomains in order to exploit parallelism. A few methods of this category are *refine* [27, 28] *EPIC* [29] *Feflo.a* [30], *avro* [31, 32], and the method presented in [33].

*refine*, *EPIC*, *avro* and [33], decompose the mesh using graph-based methods and “freeze” the elements along subdomain boundaries during adaptation. Mesh operations are applied only to internal elements. Several element migration passes allow the fixed elements to become internal and also give the opportunity of load balancing.

*Feflo.a* [30] approaches the discrete domain decomposition problem using a hierarchical partitioning technique combined with a region-grow greedy algorithm. In particular, the initial mesh is partitioned based on a breadth-first approach. The internal elements are adapted while the subdomain boundary elements remain fixed. In the next iteration the fixed elements are partitioned and become the new subdomain while their common boundaries become fixed etc.

When it comes to the repertoire of operations, *refine* and *EPIC* utilize edge-split, edge-collapse, edge-face swap, and vertex smoothing. On the other hand, *Feflo.a*, *avro* and [33] use a cavity-based approach that allows using a single operator to express all the above mesh operations. This feature not only simplifies implementation and maintenance but in the case of *avro* it enables performing mesh adaptation in higher dimensions [34]. When it comes to [33] the cavity-based criterion combines both element size and element quality into a single criterion instead of utilizing separate operator passes.

Our method, *CDT3D*, utilizes the same elementary operations but employs no domain decomposition or intensive data decomposition like the above adaptive methods. Instead, it applies the speculative approach to exploit parallelism and decompose data on the fly. Also, in contrast to previous speculative methods that arose from the telescopic approach such as [13, 17] the proposed approach includes a variety of different mesh operations instead of just the Delaunay kernel. To the authors' best knowledge, the method of this work is the first tightly-coupled speculative fine-grained method for anisotropic 3D mesh adaptation for shared-memory architectures.

### 3 Metric-based Adaptation within the *CDT3D* library

The metric-based approach of this work builds on top of *CDT3D* [35], a mesh generation toolkit developed at the CRTC lab<sup>1</sup> of Old Dominion University. *CDT3D* has demonstrated significant improvements in end-user-productivity compared to state-of-the-art isotropic advancing front mesh generator [36]. Its modular design allowed the addition of refinement zones for the isotropic method that enable its use in Large Eddy Simulations as presented in [37]. When faced with the challenge of introducing metric-based adaptation capabilities, we opted to decompose each mesh operation into *topological* and *geometrical* components. Topological steps access and modify only the connectivity information (a 2-3 flip, for example, see Figure 2a) and as such, there is no need for modifications for metric adaptation. On the other hand, geometrical steps, such as evaluating a predicate that decides whether a flip should be performed, will need to incorporate the metric information. Figure 1 depicts the metric-adaptive pipeline built and evaluated throughout this work. In the rest of the section we iterate through the diagram discussing the most significant contributions required to enable metric adaptation in *CDT3D* and introduce support for handling CAD-based information. Moreover, to improve the end-user-productivity of *CDT3D* the speculative fine-grained scheme presented in [36] is adapted to handle all the mesh operations utilized in the pipeline. The next sections present technical details of each of the parallel operations.

---

<sup>1</sup><https://crtc.cs.odu.edu> (Accessed 2023-03-30).

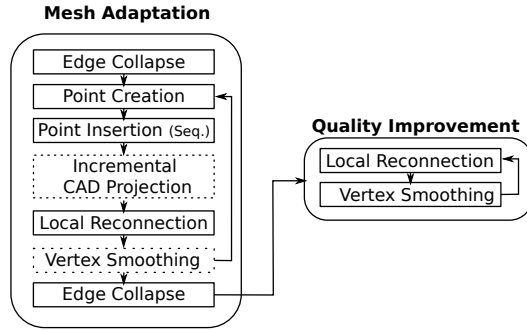


**Fig. 1:** Pipeline of the presented approach. Dotted modules are utilized only when CAD data are available.

### 3.1 Parallel Speculative Local Reconnection in Metric Spaces

The fine-grained speculative scheme for local reconnection employed by *CDT3D* has been already presented in detail in [36]. We provide here only the contributions pertinent to metric-based mesh adaptation.

A local reconnection pass consists of four types of flips [38] depicted in Figure 2. The flip operations are purely topological transformations, however, the criteria they use are based on geometrical quantities, and as such, they need to be substantially enhanced in order to incorporate metric-based information. The first criterion used in conjunction with a 2-3/3-2 flip is Delaunay-based: face  $abc$  will be replaced with edge  $ed$  if  $d$  is in the circumsphere of  $abc$  (see Figure 2a). Extensions of the Delaunay criterion for metric spaces has been suggested in reference [39] where the authors provide approximations of the criterion based on the *Delaunay measure* which is defined as follows: Let  $K = (x_1, x_2, x_3, x_4)$  be a tetrahedron, the Delaunay measure of a point  $p$  with respect to  $K$  is defined as:

$$\alpha_{\mathcal{M}}(p, K) = \frac{d_{\mathcal{M}}(O_K, p)}{d_{\mathcal{M}}(O_K, x_1)} \quad (1)$$

where,  $O_K$  is the circumcenter of  $K$  evaluated in metric  $\mathcal{M}$ . If  $\alpha_{\mathcal{M}}(p, K) < 1$  then  $p$  is in the circumsphere of  $K$ . Notice that we did not specify  $\mathcal{M}$  explicitly. In fact, by incorporating the metric from 1, 2 or even all 4 points of  $K$  one can get better approximations of the Delaunay criterion [39]. In this work, we adopt the criterion presented in [40], that uses not only metric information of  $K$  but also of the point  $p$  itself:

$$\begin{cases} \alpha_{\mathcal{M}_p}(p, K) < 1 \\ \sum_{i=1}^4 \alpha_{\mathcal{M}_{x_i}}(p, K) + \alpha_{\mathcal{M}_p}(p, K) < 5 \end{cases} \quad (2)$$

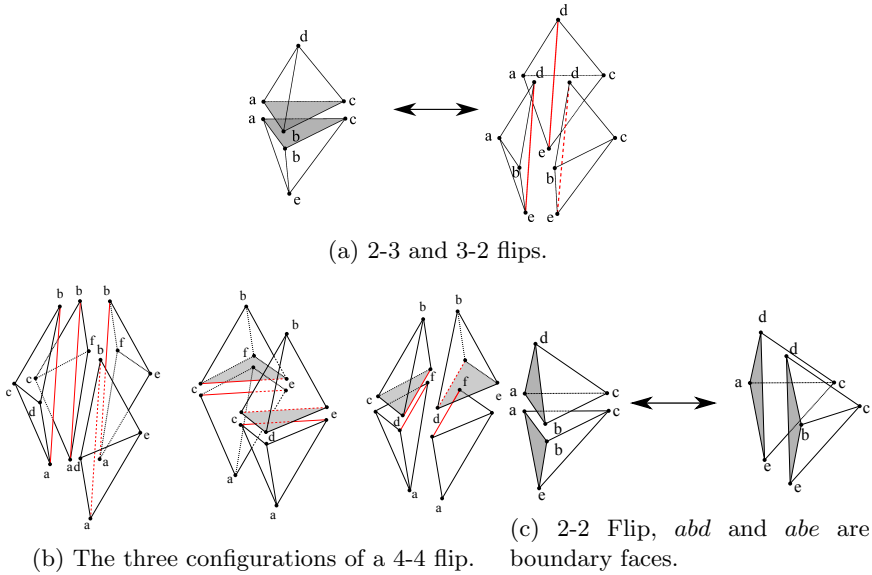


**Fig. 2:** Topological Flips utilized by *CDT3D* for local reconnection.

In practice, this criterion consists of evaluating the traditional Delaunay criterion in 5 different spaces equipped with a different (but constant each time) metric and averaging the results. Similarly, in order to optimize the connectivity on the surface of the mesh, a 3D in-circle test is coupled with a 2-2 Flip. In particular, a surface edge  $ab$  is flipped for  $ed$  if  $d$  is in the circumcircle of  $abc$  (see Figure 2c).

The second criterion used is the maximization of the minimum Laplacian edge weight of an element  $K$  [41]. This criterion is combined with the 2-3/3-2 and the 4-4 Flips (see Figure 2a and 2b). In isotropic mesh generation it consists in evaluating the following quantity:

$$Q(K) = \max_{i=1\dots 6} \frac{\langle n_{F_{i,1}}, n_{F_{i,2}} \rangle}{6|K|}$$

where  $F_{i,1}, F_{i,2}$  are the two faces attached to the  $i$ -th edge of a tetrahedron  $K$ ,  $n_{F_{i,1}}, n_{F_{i,2}}$  the respective face normals and  $|K|$  the volume of  $K$ . The algorithm performs a flip only if the new configuration increases this quantity. For the anisotropic case, the formula is adapted using a metric tensor  $\mathcal{M}$  interpolated at the centroid of  $K$ . Moreover, in order to avoid the numerically expensive evaluation of the normals, the formula is replaced with an equivalent formula presented in [42] that uses only inner products between the edge vectors of each face:

$$Q_{\mathcal{M}}(K) = \max_{i=1\dots 6} \frac{\langle e_i, e_j \rangle_{\mathcal{M}} \cdot \langle e_i, e_k \rangle_{\mathcal{M}} - \langle e_i, e_i \rangle_{\mathcal{M}} \cdot \langle e_j, e_k \rangle_{\mathcal{M}}}{6|K|_{\mathcal{M}}} \quad (3)$$

### 3.2 Parallel Point Creation for Anisotropic Mesh Adaptation

The parallel implementation of the point creation kernel is structured in a similar fashion to the local reconnection kernel. Each thread iterates a subset of elements that do not satisfy the local length criteria in order to generate *candidate* points for insertion. New candidate points are compared against existing mesh vertices and other candidates for proximity (in the metric space). This check allows to avoid the creation of points too close to each other that will impact the quality and the local size requirements. A similar approach named *Anisotropic Filtering* is presented in [43]. Once a point passes all proximity tests it is stored in a list assigned to the contained element. Storing the candidate points in the contained element gives a significant advantage; both the proximity checks and the subsequent point insertion step (see Figure 1) can be performed in constant time since the point location step of the direct insertion kernel will only require constant time to execute.

In contrast to local reconnection, the point creation step does not perform any topological modification and thus no cavity locks are required. Moreover, vertices are allocated into thread-local memory pools [44] and thus vertex allocation can be performed concurrently. The only step that requires synchronization is adding the candidate point to the list of the contained element. Our experiments showed that this lock is short-lived and the use of spinlocks is a sufficiently efficient solution to handle concurrent accesses.

Our approach uses a centroid-based point-creation method. This method will check the edge lengths of an element that does not meet the quality criteria in the metric space, and if any of them does not satisfy the spacing requirements, it will generate its centroid as an initial candidate point. If the tetrahedron has a boundary face, or if any of its edges is a ridge (i.e., lays between two different surface markers) encroachment rules similar to those used in Constrained Delaunay refinement [45] are utilized. In particular, the candidate point will be checked for encroachment (in the metric space) against the boundary face, and if encroachment occurs, the candidate is rejected and the centroid of the boundary face becomes the new candidate. The same procedure is applied to the new point which is checked for encroachment against any ridge edges, see Figure B1 in Appendix B for more details. Once a candidate is created, the metric is interpolated using formula (A3). Inspired by [46], we store alongside the metric value at a point  $\mathcal{M}(p)$  its logarithm  $\log(\mathcal{M}(p))$ . Although this requires more space, it reduces significantly the time required for metric interpolation.

### 3.3 Speculative Edge Collapse for Metric-based Adaptation

The goal of the edge collapse operation is to suppress edges with lengths smaller than a target value. In this work, the edge collapse operation is utilized as

---

<sup>1</sup>Parallel implementation was developed in collaboration with Fotis Drakopoulos.

a pre- and post-refinement operation (see Figure 1). The pre-refinement step removes short edges present in the input mesh. By default an edge is considered short if it is smaller than  $1/\sqrt{2}$  as measured by (A1). Depending on the input mesh, the user may increase this value in order to create a coarser initial mesh which can lead to a better quality of the final mesh as we demonstrated in [9]. The post-refinement use of the operation allows the removal of any short edges created during refinement.

The parallel implementation of the edge coarsening the algorithm iterates through the vertices allocated by each thread and exploits parallelism utilizing a `#pragma omp parallel for schedule(guided)` OpenMP construct. Each thread picks and locks (speculatively) the vertex ( $a$  in Figure 3) corresponding to the iterator value. Then it speculatively locks its adjacent vertices (blue in Figure 3). If any of the locks fail, the thread will release any acquired locks and it will proceed to the next vertex. Notice that locking the vertices implicitly grants exclusive access to all their adjacent tetrahedra (red elements of Figure 3). Once the required locks have been acquired, the edge lengths between the vertex  $a$  and the rest of the vertices of its cavity are evaluated. If an edge with a length less than a user-defined value is found then the edge will be collapsed. Additional criteria such as not applying edge collapse in cases that will increase the surface deviation (see Section 4) are also applied for edges on the surface of the mesh. Finally, the edge is collapsed by moving the second point to the first. The `guided` scheduler was selected because it performs on average better for cases that require different levels of coarsening [9]. More sophisticated parallel iteration and tasking schemes are out the scope of this work but have been explored in [47].

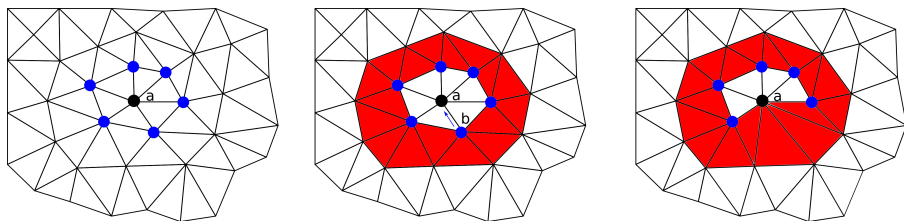


**Fig. 3:** Steps of speculative edge collapse.

### 3.4 Vertex Smoothing

During the Quality Improvement step of the isotropic mesh generation pipeline of *CDT3D* the user can use a combination of Laplacian [48] and optimal point placement smoothing [35]. Utilizing these methods for metric-based adaptation did not yield a substantial improvement in mesh quality while, on the other hand, adding a significant overhead in the running time. As an alternative, a different vertex relocation strategy was employed. First, only vertices with at least one attached element that has a mean ratio shape measure (equation

(A6)) below 0.1 are considered. This value is based upon common practices present in the literature [49, 9]. Moreover, a non-smooth optimization method similar to the one presented in [50] was employed by optimizing the minimum value of the mean ratio measure among all the elements attached to the vertex. For simplicity, the current implementation does not utilize the integer programming-based solution presented in [50] or the computation of the active set of the gradients used in [51] in order to determine the optimal search direction. Instead, it uses a reduced search space comprised by the segments that connect the vertex to be relocated with the centroids of the faces of its cavity (see Figure 4 left). This search space was found to be sufficient for the cases of this study. Once the search space is determined, the vertex will be moved incrementally along all the search directions and the position that optimizes the quality will be selected.

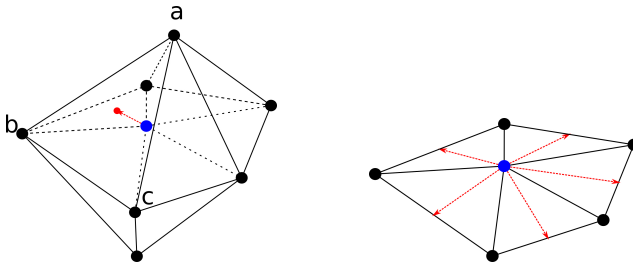


**Fig. 4:** Search Space for Smoothing Operation.

For vertices lying on the surface, the search space is constrained to the segments that connect the moving vertex to the midpoints of the edges of the corresponding surface cavity (see Figure 4 right). If the vertex lies on a ridge the search directions are only two; toward either end of the ridge. Along with the optimization criterion, the method always ensures that no elements are inverted and thus no subsequent untangling step is needed. When it comes to speculative execution, vertex smoothing follows a similar approach to edge collapse.

### 3.5 Effect of the complete set of operations

During the process of developing metric-based adaptation in *CDT3D* we often wondered if the full suite of operations was indeed required in order to achieve reasonable results. Figure 5 compares an early implementation of the method presented in [52] along with the current version compared with other state-of-the-art mesh adaptation methods [9]. The earlier attempt utilized an external tool for surface adaptation and created an initial mesh by means of boundary recovery. The mesh was then adapted using metric-based local reconnection only for the inner volume elements with no other metric-aware operation. During the procedure, the surface mesh was kept fixed. The ability to adapt

the boundary of the mesh at the same time as the volume mesh, along with the vertex smoothing operation and the addition of a metric-based edge collapse enhanced the quality of the generated mesh by 3 orders of magnitude (as measured by the mean ratio shape measure (A6)) with respect to our initial attempt.

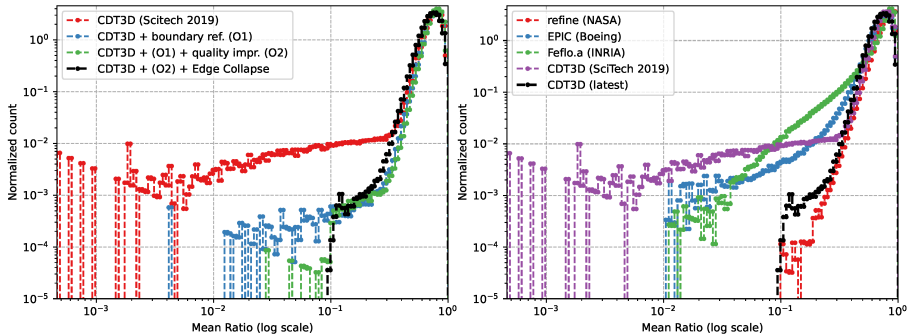


**Fig. 5:** Left: The effect of adding more metric-aware operations. Right: The improved approach versus our previous results presented in [52].

## 4 Handling Geometry through metric spaces

Industrial applications as well as several high-quality research-focused workshops such as the High-Lift prediction workshop<sup>2</sup>, the International Workshop on High-Order CFD Methods<sup>3</sup>, the Sonic Boom Prediction Workshop<sup>4</sup>, and the Geometry and Mesh Generation workshop<sup>5</sup> make extensive use of analytical/geometrical descriptions of the domain. These descriptions are of particular importance since many flow quantities of interest depend on the exact shape characteristics of the components which could be lost in a discrete model. Thus building a mesh based on the geometrical description of the domain is essential for these studies. Moreover, accessing geometrical information while adapting the mesh leads to better domain discretization and thus more accurate solution.

There are many methods that can be used to build this representation but traditionally CFD simulations, and the engineering community in general, leaned towards the use of the Boundary Representation method (BREP or B-rep) [53]. The B-rep method uses a combination of topological entities (Faces, Edges, and Vertices) along with their geometrical description as (analytic) surfaces, curves, and points. B-rep data can also hold boolean operations such as intersection and union between entities as well as higher-level operations

<sup>2</sup><https://hiliftpw.larc.nasa.gov> (Accessed 2023-04-25).

<sup>3</sup><https://how5.cenaero.be> (Accessed 2023-04-25).

<sup>4</sup><https://lbpw.larc.nasa.gov> (Accessed 2023-04-25).

<sup>5</sup><http://www.gmgworkshop.com> (Accessed 2023-04-25), Internet Archive <https://web.archive.org/web/20230407233207/https://www.gmgworkshop.com/> (Accessed 2024-04-06).

such as extrusion and sweeping [54]. B-rep data are usually handled by a Computer-Aided Design (CAD) kernel which is responsible both for generating B-rep data and performing queries to them.

The authors of [55] describe in detail two approaches that can be used to incorporate geometrical information to a meshing procedure. The first option is to build a surrogate geometry by constructing a discrete, often high-order, surface mesh that captures all the features of the input geometry at a desired resolution. This approach has the advantage of controlling the fidelity of the constructed representation. Also, it allows fixing inconsistencies of the continuous representation that can occur due to different tolerances of each continuous patch. One can construct a surrogate geometry even when a geometrical description is not available based on the input surface mesh. This approach is currently utilized by the *Feflo.a* and *EPIC* mesh adaptation software [55] (among others).

The second approach, which is used in this work, is to maintain an association between each boundary vertex of the mesh and its adjacent geometric entities. This approach allows querying the appropriate Geometrical entity through the CAD kernel. It has the disadvantage of inheriting the issues present in the B-rep model but, it provides access to the CAD kernel in a simple manner. Moreover, it aligns better with our goal which is to introduce preliminary support for B-rep data to our mesh adaptation method. Currently, this approach is also favored by the *refine* mesh mechanics suite [56] and *avro* [32]. In practice, we introduced at each mesh vertex a pointer to the lowest dimension geometric entity that is adjacent. This information together with topological and geometrical queries to the geometry kernel allows to evaluate  $uv$  (or  $t$ ) parametric coordinates for any mesh vertex. The current implementation makes use of the EGADS geometry kernel [57] through a generic API which could be adapted for another CAD kernel in the future.

Geometry information is used throughout the mesh adaptation procedure in several ways. First, newly introduced boundary points are projected to the surface using a dedicated module (see Figure 1) right after vertex insertion. The projection of a mesh vertex  $p$  is evaluated by first querying the kernel for the closest point  $p'$  of the B-rep. The mesh vertex  $p$  is then relocated to  $p'$  only if this operation does not create any inverted elements attached to vertex  $p$ . If it does, we try to move  $p$  to  $(p + p')/2$ , i.e., the midpoint between the two points. This procedure is applied iteratively until we find a valid position or reach a recursion limit which we set to 5. Mesh vertices that were placed in an intermediate position are recorded and they are included for projection in the next iteration of the algorithm. The local reconnection that will be applied in the vicinity of point  $p$  may enable moving the point closer to its projection in a subsequent iteration. Projecting a mesh vertex to the B-rep involves a Newton-Raphson root finding method and therefore its speed and final solution depend heavily on the initial guess of the projected point. To speed up the procedure, we approximate the  $uv$  (or  $t$ ) parameters of a newly created point during the point creation module based on the average of the

$uv$  (or  $t$ ) values of the vertices belonging to the triangle or edge being split. These approximate  $uv$  (or  $t$ ) parameters are then cached for this point and it is used as an initial guess during the next projection stage.

Information on the analytic expression of the underlying surface is also used to minimize the deviation of the discrete surface mesh from its analytic description. In practice, the deviation is evaluated as the dot product between the normal of a discrete triangle and the normal of the geometry surface evaluated at the centroid of discrete triangle [55], (see also Figure 6). The deviation is minimized as part of the local reconnection pass (see Figure 1) using 2-2 Flips (see Figure 2c). The Edge Collapse operation can also use deviation of the surface cavity from the analytic surface as an extra quality criterion when deciding whether a surface edge should be collapsed. Controlling the deviation not only produces a mesh that approximates the surface better, but makes the operations more robust avoiding cases that will lead to a tangled mesh.

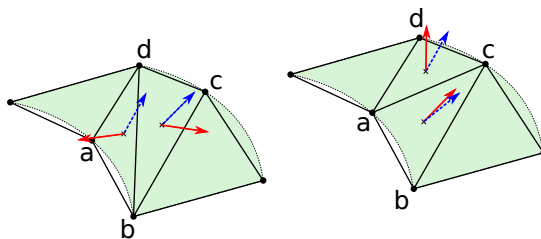


**Fig. 6:** Deviation Improvement. A flip of the edge  $bd$  for  $ac$  reduces the deviation between the discrete normals (red solid vectors) and the analytic normals computed at the centroids of the triangles (blue dashed vectors).

When utilizing CAD projection, we also found it beneficial to perform vertex smoothing at the end of the adaptive iteration (see Figure 1) allowing to improve the quality of the vicinity of the projected vertices.

## 5 Evaluation

*CDT3D* has been already compared in the literature to state-of-the-art methods in terms of both mesh quality and scalability. In particular, the analysis presented in [9] indicates that *CDT3D* offers competitive mesh quality and scales well within a single shared-memory node.

In contrast to our previous work that focused mainly on element quality measures, we compiled a suite of cases that help re-focusing on the main goal of mesh adaptation: capturing features of the underlying simulation. At the same time, we test how well *CDT3D* operates as a part of an adaptive pipeline composed of open-source components that include a CFD solver and publicly available test cases enabling thus future comparisons with other methods.

Section 5.1 describes the setup of our adaptive pipeline in terms of software as well as data flow between the various components. The test cases are of

increasing difficulty and focus on different aspects of *CDT3D*. First, in section 5.2 the adaptation procedure is verified by adapting meshes based on analytic scalar fields. Then, section 5.3 presents results of *CDT3D* with a CFD solver and a laminar flow case that involves a piece-wise linear geometry. Section 5.4 increases the difficulty by introducing curved geometry and solving an inviscid flow. As a stress test in section 5.5 we use *CDT3D* to perform an analysis of a turbulent flow over a complex geometry. To provide a complete picture of *CDT3D* characteristics we perform a detailed speedup and efficiency analysis of each operation in section 5.6.

The adaptation is performed using the multiscale metric [4] which is a feature-based approach that controls the  $L^p$  norm of the interpolation error of a user-defined scalar variable. The metric field is evaluated using the  $L^2$  projection scheme provided by *refine* [28] software suite. The final step in constructing a metric field is the application of gradation. The gradation aims at putting constraints over the largest size deduced from a metric and smoothing the metric transition between edge-connected vertices. In this work we adopt the *mixed-space-gradation* method presented in [58] and utilize its implementation in *refine* [56].

The cases that utilize a CFD solver use SU2 7.0.6 [59], version 1.18 of EGADS is used while for *refine* we used version 1.9.4-d3ffb79d28. ParaView was used to visualize results that involve meshes, FreeCAD was used to visualize geometry, and matplotlib was used for the 2D plots.

## 5.1 Experimental Setup

In order to meet the ever-evolving and growing demands of the CFD community, a simulation pipeline should be able to integrate a plethora of different tools. The T-infinity project [60] demonstrates a series of different use cases where a high-level Python interface can be used to build sophisticated pipelines. In this work, we focus on a single pipeline depicted in Figure 7 which is pertinent to mesh adaptation.

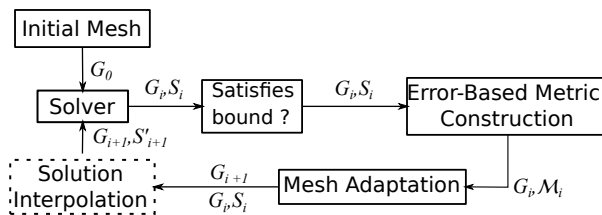


**Fig. 7:** Mesh Adaptation pipeline.  $G_i$  denotes the mesh at the  $i$ -th iteration.  $S_i, S'_i$  is the solver solution and the interpolated solution at the vertices of  $G_i$ , respectively.  $M_i$  corresponds to the metric field associated with the vertices of  $G_i$  and derived from  $S_i$ .

In Figure 7, the process is initialized with a (usually coarse) mesh  $G_0$  that captures all the geometrical features of the input model at some user-defined accuracy. The solver then evaluates a discrete solution of the problem of interest and stores it in each mesh element. For simplicity, we assume that the solver in this case is vertex-based and the solution is stored at each vertex of the mesh  $S_i$ . The next block captures a user-defined condition that controls the exit of the iterative process. It can be based on some target simulation quantity or on the total number of iterations of the adaptive loop. The Metric Construction step creates a metric field  $\mathcal{M}_i$  at each vertex of  $G_i$  using  $S_i$  that drives the adaptation process. Mesh Adaptation modifies the mesh based on the provided metric field and generates a new mesh  $G_{i+1}$ . Optionally, one can interpolate the solution of the previous iteration to the new mesh thus producing  $S'_{i+1}$ . This step allows the solver to restart the calculation from a state closer to the converged solution instead of the freestream conditions which is the default. Finally, the new mesh (and optionally the interpolated solution  $S'_{i+1}$ ) are passed to the solver for the next iteration of the loop.

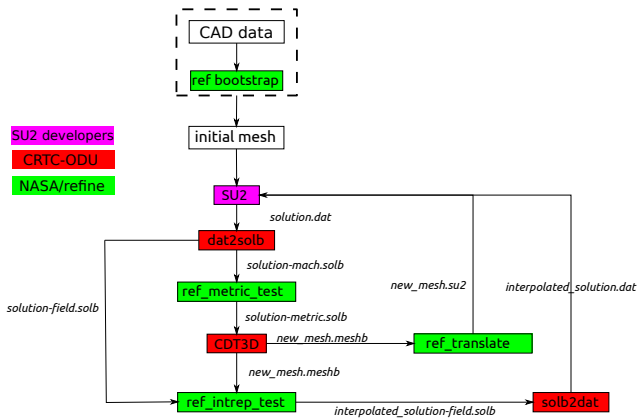


**Fig. 8:** Software pipeline utilized in the adaptive pipelines of this study.

The corresponding software pipeline can be seen in Figure 8. For the cases of this study, the input volume mesh is either given or created out of a CAD file using `ref bootstrap` which is part of the `refine` mesh mechanics suite[56]. `ref bootstrap` uses the EGADS [57] kernel in order to generate an initial surface triangulation of the input CAD file. The surface mesh is then adapted based on the curvature and other geometrical features. Adapting the surface in the absence of a volume mesh gives greater flexibility since the software is not constrained by the requirement of conformity to a volume after each operation. A volume mesh is then generated using an external tool such as TetGen [61] or AFLR [62] and finally the volume mesh is adapted based on a metric field derived by the geometrical features of the CAD input. SU2 will then produce a solution file that holds values of

the discrete solution at each vertex of the input mesh. `dat2solb` is used to convert the solution to a libMeshb-compatible file [63]. The extracted Mach field (`solution-mach.solb`) is then passed to `ref_metric_test` that creates a multiscale metric field based on it (`solution-metric.solb`). The multiscale metric field can be optionally intersected with a curvature- and feature-based metric built based on the geometrical features of the input model. *CDT3D* will then use the metric field along with the mesh used by *SU2* to generate an adapted mesh (`new_mesh.meshb`). If solution interpolation is utilized, we pass the new mesh along with a `.solb` version of the *SU2* solution to `ref_intrep_test` which we then convert using `solb2dat` to an *SU2*-compatible file (`interpolated_solution.dat`). The values of the previous solution are interpolated using linear interpolation. Finally, the adapted mesh is passed to *SU2* after being converted to a `.su2` mesh file along with the interpolated solution if this was generated.

It should be noted that the metric field can be built using any solution variable besides the local Mach number<sup>6</sup>. However, the use of the local Mach number is favored in the literature, since it provides a “compound” scalar variable that varies in most flow regions, thus allowing us to capture most of the flow features [64, 65].

Since the solver, a major part of the pipeline is an external and sophisticated project, fine-tuning its parameters and detailed convergence and error-analysis is outside the scope of this work. Instead, the goal of this section is to show the capability of our method to function as part of an adaptive pipeline.

## 5.2 Analytic scalar fields

The adaptation pipeline of Figure 7 has many components and the errors in each one can have accumulative and unpredictable effects in the final calculation. In an effort to mitigate these issues, we first test *CDT3D* by replacing the CFD solver with analytic metric fields. In particular, instead of solving a flow problem at each iteration, we evaluate an analytic function at the vertices of the mesh. The adaptive iterations will create a mesh that is expected to drive the interpolation error down. For this test, we will be using the three analytic cases of the benchmark described in [66] and implemented in the *refine* suite. The multiscale metric implementation of *refine* has been combined with several mesh adaptation tools and verified separately in [66] and thus, we will only focus on the verification of the adaptation procedure in *CDT3D*.

For each of the three analytic scalar fields ((4),(5),(6)) the adaptation pipeline starts with a uniform tetrahedral mesh of the unit cube domain  $[0, 1] \times [0, 1] \times [0, 1]$  with 64 vertices. In each subsequent iteration, a multiscale metric field is computed using  $F(x, y, z)$  as a scalar field. The metric is computed in the 2-norm and the gradation value is set to 3. The metric is then

---

<sup>6</sup>The local Mach number is defined as the ratio of the local flow speed over the local speed of sound.

passed to our method along with the mesh of the previous iteration with the goal of adapting the previous mesh to the new metric field.

$$\text{sinfun3} := F(x, y, z) = \begin{cases} 0.1 \sin(50xyz) & \text{if } xyz \leq \frac{1}{50}\pi \\ \sin(50xyz) & \text{if } xyz \leq \frac{2}{50}\pi \\ 0.1 \sin(50xyz) & \text{else} \end{cases},$$

$$\text{where } xyz = (x - 0.4)(y - 0.4)(z - 0.4) \quad (4)$$

$$\text{tanh3} := F(x, y, z) = \tanh((x + 1.3)^{20}(y - 0.3)^9 z) \quad (5)$$

$$\text{sinatan3} := F(x, y, z) = 0.1 \sin(50xz) + \tan^{-1}(0.1/(\sin(5y) - 2xz)) \quad (6)$$

For each field, 90 adaptive iterations are performed with the metric complexity (see equation (A4)) increased at every 10 iterations. The convergence plots in Figure 9 show the interpolation error of the last 5 iterations at each complexity with respect to the finest generated mesh. Since, the multiscale metric approximates linear interpolation error via a Hessian reconstruction, all results are expected to exhibit second-order convergence rate. For comparison, the same adaptation procedure was performed using *refine*.

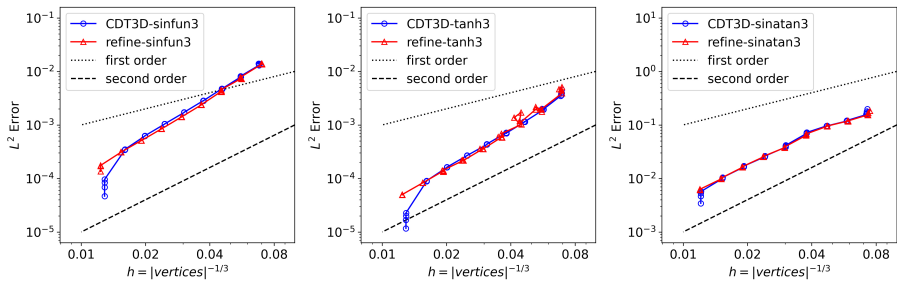


**Fig. 9:** Convergence rates for *CDT3D* and *refine* for the three scalar fields.

Figure 9 indicates that the convergence rate of *CDT3D* matches closely the rate of *refine* and they both exhibit 2nd-order convergence. Figure 10 presents the adapted meshes. *CDT3D* is able to recover the features of the scalar fields at both small and large scales.

### 5.3 Laminar Subsonic Flow over a Delta Wing

For the next case, *CDT3D* is coupled with an adaptive pipeline that includes a CFD solver. The input geometry is a delta wing with planar faces. The 3D delta wing simulation conditions have been set so that they match the case used in the first three High-Order Workshops [67]. This case is well studied in the literature and it is preferred due to its simple geometry and yet non-trivial flow features. Adaptive results in terms of multiblock meshes appear

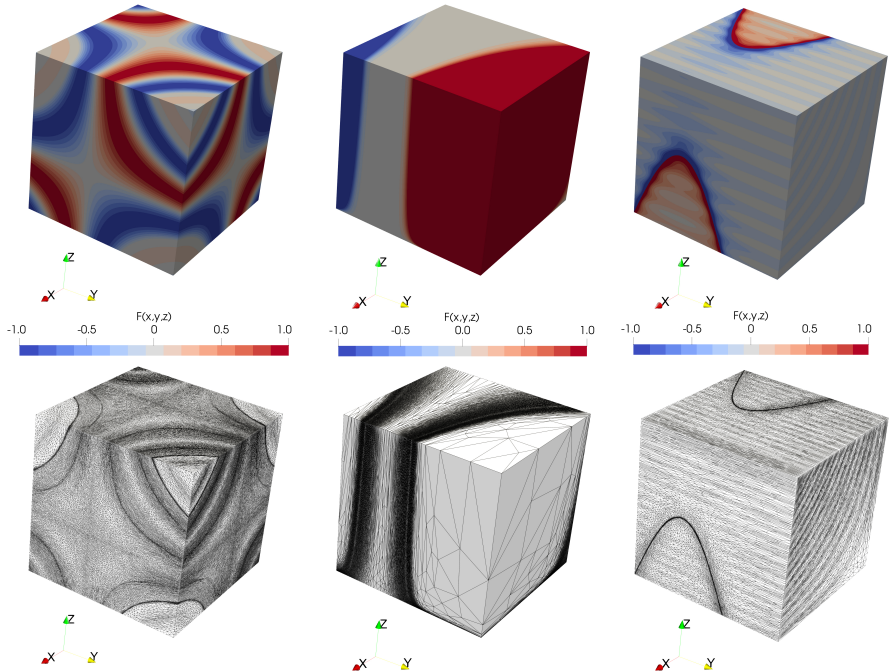


**Fig. 10:** Adapted meshes for the three fields. Top: `sinfun3`, `tanh3` and `sinatan3` fields. Bottom: Corresponding *CDT3D* adapted meshes at 256,000 target complexity.

in [68], verification results for the multiscale, MOESS and output-based metrics appear in [66] and [69].

The freestream conditions are 0.3 Mach, 4000 Reynolds number based on a unit root chord length and  $12.5^\circ$  angle of attack. The wing surface is modeled as an isothermal no-slip boundary with the freestream temperature equal to 273.15K. The Prandtl number is 0.72 and the viscosity is assumed constant. SU2 is configured with an initial CFL number of 1 and a final value of 5 with a ramping of 1.001. As a linear solver, FGMRES is used with the ILU preconditioner. The error for the linear solver is set to  $10^{-10}$  and the number of the linear iterations to 10. The Roe convective scheme is used with MUSCL reconstruction and the Van Albada edge limiter.

For each iteration except the first, we also supplied an interpolated solution on the new mesh based on the solution of the previous iteration. The metric is constructed based on the local Mach field of the solution and the metric gradation value is set to 2.0. The complexity of the metric (as defined by (A4)) is doubled every 5 iterations. The solution-based metric is intersected also with a curvature- and feature-based metric built based on the geometrical features of the wing. Although the geometry, in this case, is

planar, the CAD kernel is utilized to validate its implementation and coupling with *CDT3D*. We considered 7 metric complexity values for this study: [50 000, 100 000, 200 000, 400 000, 800 000, 1 600 000, 3 200 000].

Figure 11 depicts the initial surface mesh of the delta wing as well as adapted meshes at 100,000 and 800,000 complexity respectively. The initial mesh has 901 vertices, the middle corresponds to the 15th iteration with 377,569 vertices and the last corresponds to the 25th iteration and has 1,467,922 vertices. Figure 12 depicts streamlines and contour slices of the final solution.

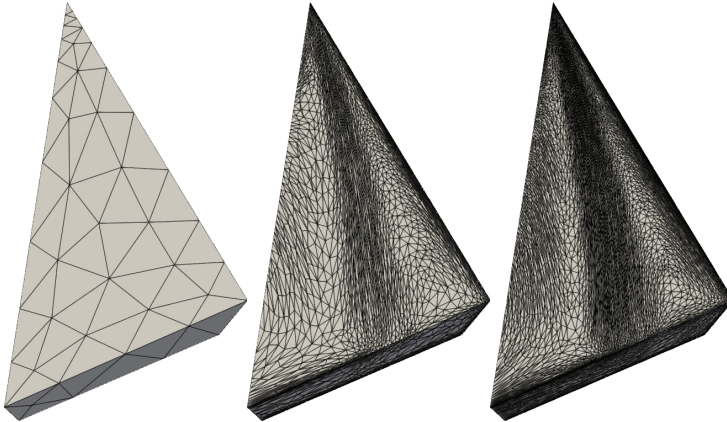


**Fig. 11:** Adapted mesh at three different complexities. Left: Initial mesh, Middle: mesh at 100,000 complexity, Right: mesh at 800,000 complexity.

To access the quality of the results of the adaptation procedure and its coupling with *CDT3D*, drag and lift coefficients are compared against the results presented in [68, 70], and [66]. Figure 13 presents the results. Both the drag and the lift coefficients are within less than 0.55% of all the reference values. The final values as evaluated by SU2 on the 35th iteration are  $C_D = 0.165396$  and  $C_L = 0.346937$ .

When it comes to execution time, we collected the time required for the solver and *CDT3D* which are the dominant components of the adaptation pipeline. Table 1 presents performance data for every 5 iterations of the adaptive pipeline. SU2 is deployed on the ODU's `turing` cluster<sup>7</sup> that houses nodes with a variety of different specifications. The number of cores used by the solver was set so that it corresponds to about 10,000 vertices per core and it was constrained to 300 to reduce the waiting time in the job scheduler queue of the cluster. *CDT3D* is using one of `turing`'s nodes with two sockets each one with a Intel<sup>®</sup>Xeon<sup>®</sup>CPU E5-2698 v3 @ 2.30GHz (16 cores) for a total of 32 cores.

---

<sup>7</sup><https://wiki.hpc.odu.edu/en/Cluster/Turing> (Accessed 2023-05-06).

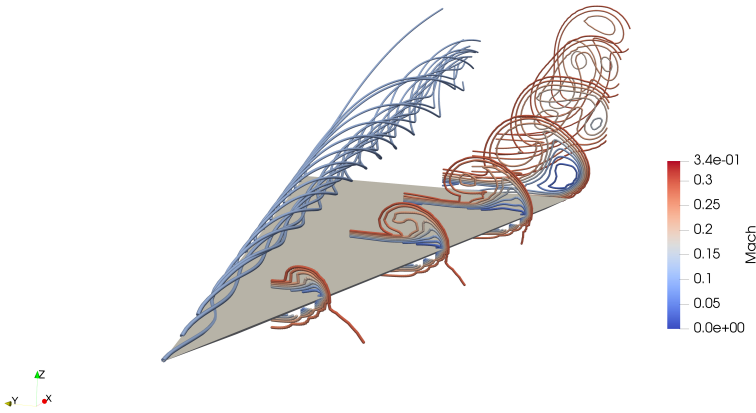


**Fig. 12:** Streamlines and Contour slices of the Mach number of the solution. (Simulation performed on the half model).

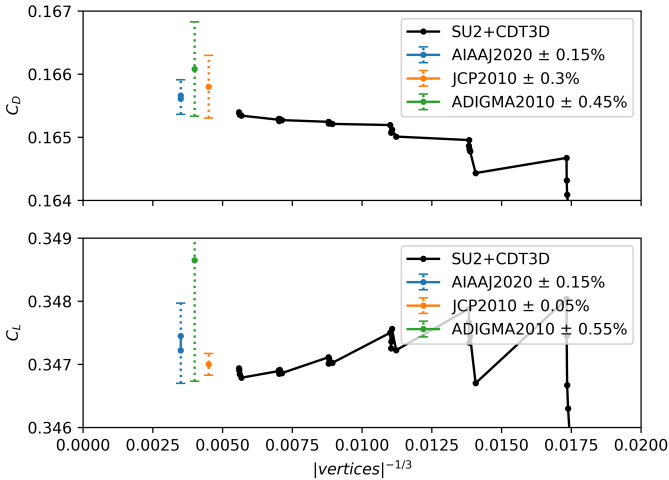


**Fig. 13:** Lift and drag coefficients as evaluated by SU2 compared against results presented in [66](AIAA2020) [68](JCP2010) and [70](ADIGMA2010).

To ease the comparison that involves different core counts and hardware specifications, we include a *core-hours*<sup>8</sup> column. Using core-hours allows the evaluation of the performance of the application with respect to the cost of

<sup>8</sup>core-hours = the number of cores used by application \* hours required for the execution.

running it on a shared cluster where charging is common to take place in terms of core-hours. The running time of *CDT3D* occupies only a small fraction of the adaptive pipeline. As mentioned in section 5.1 we used regular files to exchange data between *CDT3D* and the solver for simplicity but also to allow the solver and *CDT3D* to run on different jobs on the cluster which minimizes the total time of the experiment. The overhead of using files is small, for example in iteration 5 SU2 and *CDT3D* spent 0.18 and 0.71 seconds respectively for writing out the results, while for the last iteration the respective times are 11.16 and 86.13 seconds.

**Table 1:** Performance data of adaptive iterations.

iter.	vertices	tetrahedra	solver (s)	solver core-hours	<i>CDT3D</i> (s)	<i>CDT3D</i> core-hours
0	901	3,444	57.55	0.16	-	-
5	97,896	563,930	2,833.51	7.87	63.53	0.56
10	192,098	1,114,412	3,301.11	18.34	49.26	0.44
15	377,569	2,203,660	2,897.73	32.20	111.95	1.0
20	749,290	4,391,974	3,865.75	85.91	207.08	1.84
25	1,467,922	8,641,694	3,476.85	154.53	392.55	3.49
30	2,897,903	17,108,219	2,777.01	232.96	808.27	7.18
35	5,726,724	33,883,975	3,281.82	273.49	1622.15	14.32

## 5.4 Inviscid Onera M6 case

The next case introduces CAD data to the adaptation pipeline. We use an inviscid flow based on the description of a turbulent case included in NASA’s Turbulence Modeling Resource (TMR)<sup>9</sup>. As mentioned in NASA’s website<sup>10</sup> “*The ONERA M6 wing is a classic CFD validation case for external flows because of its simple geometry combined with complexities of transonic flow [...] It has almost become a standard for CFD codes because of its inclusion as a validation case in numerous CFD papers over the years.*” The flow conditions for this study are 3.06° angle of attack, 0.84 Mach number, and freestream temperature equal to 300K. This case utilizes the ONERA M6 wing geometry [Figure B2a](#) depicts the initial mesh generated by `ref bootstrap`.

SU2 is configured similarly to the previous case but using the JST as the convective scheme which we found to converge faster for this case. For each iteration except the first, we also supplied an interpolated solution on the new mesh based on the solution of the previous iteration. The metric is constructed based on the local Mach field of the solution and the metric gradation value is set to 10. The complexity of the metric (see equation (A4)) is doubled every 5 iterations. The solution-based metric is intersected also with a

<sup>9</sup>[https://turbmodels.larc.nasa.gov/onerawingnumerics\\_val.html](https://turbmodels.larc.nasa.gov/onerawingnumerics_val.html) (Accessed 2023-05-06).

<sup>10</sup><https://www.grc.nasa.gov/www/wind/valid/m6wing/m6wing.html> (Accessed 2023-05-06).

curvature- and the feature-based metric is built based on the geometrical features of the wing. We considered 3 metric complexity values for this study: [50 000, 100 000, 200 000].

These flow conditions produce the typical “lambda” shock along the upper surface wing. [Figure B2b](#) depicts the mesh as well as the corresponding contour plot of the local Mach number for the final iteration of the adaptive loop.

To verify our results, we compare the pressure coefficient against two different datasets from the literature. First, the experimental values of Case 2308 of [\[71\]](#) acquired from the TMR website<sup>11</sup> that corresponds to our configuration. Also, we executed SU2 with the same configuration on a structured grid generated using a custom publicly available mesh generation code [\[72\]](#) using the input parameters suggested by the TMR website<sup>12</sup>. In particular, we used the level 2 mesh (L2) that has 36,865 points across the surface of the wing. For comparison, the final mesh of our pipeline has 6,898 points across the surface of the wing. The top left subfigure in [Figure 14](#) depicts the 7 sections along which the experimental and numerical results are compared. The rest of the plots in [Figure 14](#) compares the results generated using *CDT3D* and the pipeline of [Figure 8](#), the structured mesh, and the experimental values. The  $x$  axis denotes the  $x$ -coordinate of the cross-section normalized by the local cord length of the wing. The  $y$  axis represents the local pressure coefficient which measures the pressure at a point relative to the freestream conditions. The combination of *CDT3D* with SU2 generates results very close to the experiment and the numerical solution obtained on the structured mesh. The differences with the experimental values are in part due to the inviscid method used in this simulation. We attempted to perform a viscous simulation using the same configuration but we did not succeed in obtaining converged results. Still, these results indicate that the meshes produced by *CDT3D* in the presence of simple curved geometries supplied as CAD data are suitable for inviscid calculations and the results are close to the reference values.

## 5.5 Inviscid flow over the JAXA Standard Model

As a final stress test, we use the Japan Aerospace Exploration Agency (JAXA) Standard Model (JSM). JSM was built as an attempt to study flow effects over a fairly complete configuration instead of isolated aircraft components that were commonly used. There are several experimental data available, see for example [\[73, 74, 75\]](#) but, we will focus on the use of the JSM in the context of the 3rd AIAA CFD High-Lift Prediction Workshop<sup>13</sup>. A summary of the workshop’s results appears in [\[76\]](#). In particular, we will study the case 2b which excludes the pylon and the nacelle of the original model and uses an angle-of-attack equal to  $4.36^\circ$  and a Mach number of 0.172. The JSM geometry is combined out of 200+ surfaces, modeling details of the aircraft including brackets, flaps and slats (see [Figure B3](#)).

<sup>11</sup>[https://turbmodels.larc.nasa.gov/onerawingnumerics\\_val.html](https://turbmodels.larc.nasa.gov/onerawingnumerics_val.html) (Accessed 2023-05-06).

<sup>12</sup>[https://turbmodels.larc.nasa.gov/onerawingnumerics\\_grids.html](https://turbmodels.larc.nasa.gov/onerawingnumerics_grids.html) (Accessed 2023-05-06).

<sup>13</sup><https://hiliftpw.larc.nasa.gov/index-workshop3.html> (Accessed 2023-05-06).

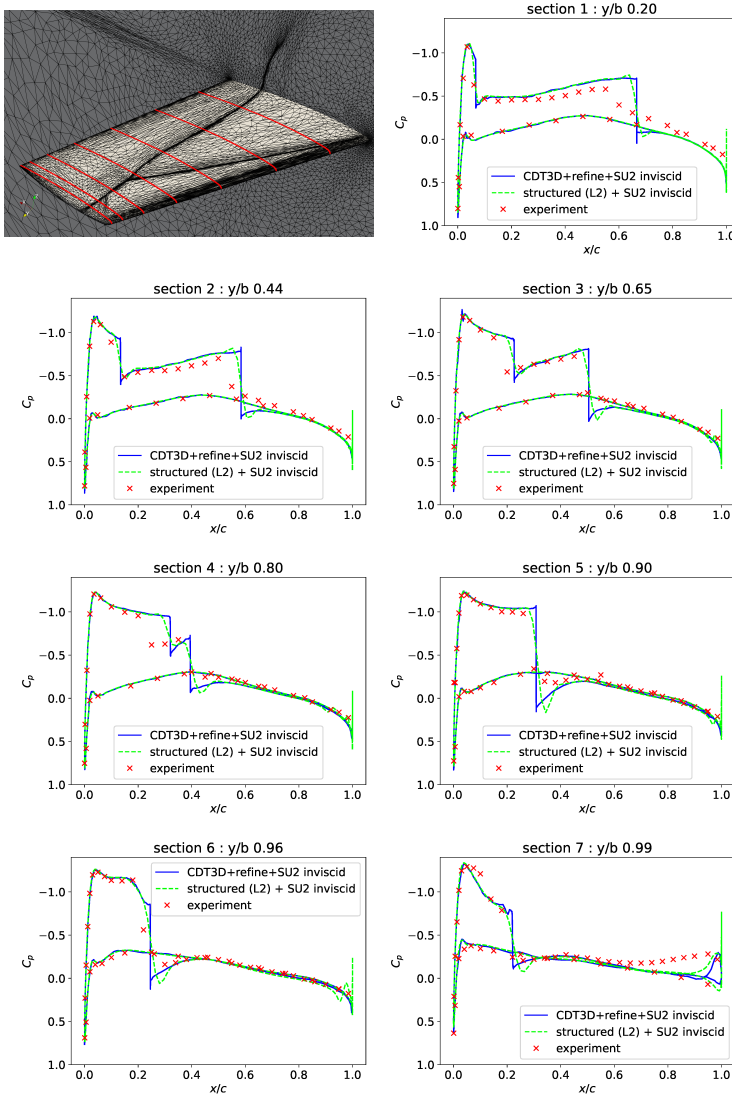


**Fig. 14:** Values of the pressure coefficient as evaluated by the solver versus the experiment across the 7 sections of the ONERAM6 wing. The location of the sections are depicted in the first figure.

SU2 is configured similarly to the inviscid ONERA M6 case of the previous section. For each iteration except the first, we also supplied an interpolated solution on the new mesh based on the solution of the previous iteration. For the first iteration, we used the coarse mesh of [Figure B4](#) of appendix [B](#) created by `ref bootstrap` of the `refine` mesh mechanics suite [56]. The

metric is constructed based on the Mach field of the solution and the metric gradation value is set to 1.5. The complexity of the metric (see equation (A4)) is doubled every 5 iterations. The solution-based metric is intersected also with a curvature- and feature-based metric built based on the geometrical features of the model. We considered 8 metric complexity values for this study: [50 000, 100 000, 200 000, 400 000, 800 000, 1 600 000, 3 200 000, 6 400 000]. The final mesh contains 13, 227, 952 vertices, 478, 518 triangles and 78, 479, 450 tetrahedra.

Figure B6 in appendix B depicts the upper surface of the wing of the final iteration along with the distribution of the local Mach number around it. Notice that the method inserts more points around the regions of higher variability of the local Mach number as expected. In particular, the wakes of the slat brackets are resolved on the upper surface. These wakes are initiated at the sharp edges of the brackets. Figure B7 depicts the final mesh along with the final solution colored by the local Mach number. Zoom-in views of one of the generated vortices are also provided.

To verify our results we compare the pressure coefficient values as evaluated by the solver against experimental results acquired from High-lift workshop website<sup>14</sup>. Figure 15a depicts the locations of  $C_p$  extraction along the wing of JSM. The rest subfigures of Figure 15 present results generated using our approach and the pipeline of Figure 8. In general, the obtained results are close to the experimental values. Notice, however, that our results overpredict the  $C_p$  values on the upper surface of the wing which corresponds to the upper section of the blue datapoints. This is in part attributed to the fact that we used an inviscid simulation instead of a viscous one. Viscous simulations were attempted starting from a coarse mesh but we didn't succeed in obtaining a converged solution. Even though we didn't investigate the reasons in depth and we are not familiar with the internal workings of SU2, we believe that these failed attempts were due to a combination of factors. First, the numerical schemes used in SU2 in combination with the complex geometry of this case might require a mesh better aligned to the geometrical features of the problem. Also, a boundary layer mesh might be required to achieve convergence for this configuration. A different solver configuration might yield better results but exploring the configuration space of the solver is out of the scope of this work. Still, this case indicates that the new functionality of *CDT3D* allows the method to handle fairly complicated CAD data in combination with solution-based metric derived from inviscid calculations.

## 5.6 Parallel Evaluation

In this section, we discuss the efficiency of our parallel implementation for the metric-based operations presented in the previous sections as well as for the end-to-end mesh adaptation process.

---

<sup>14</sup><https://hiliftpw.larc.nasa.gov/Workshop3/pressures.html> (Accessed 2021-06-17).

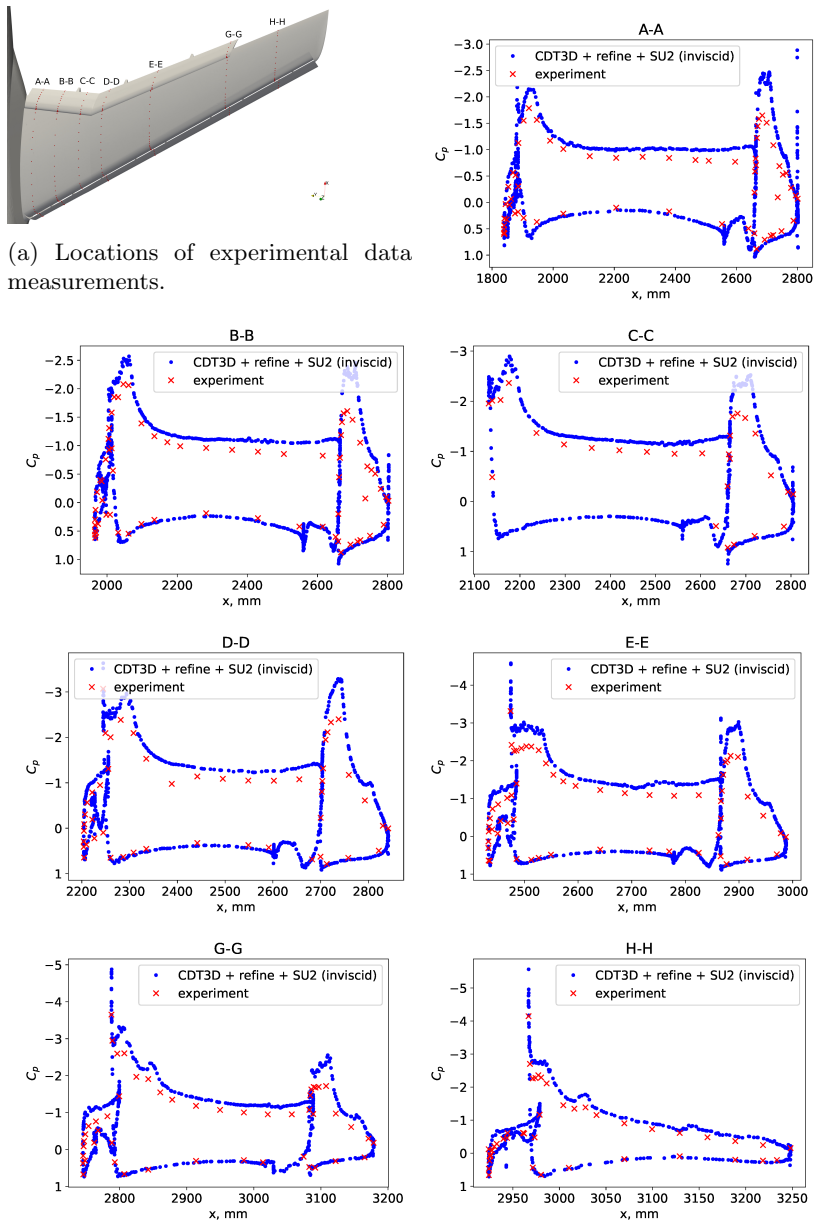


**Fig. 15:** Values of the pressure coefficient as evaluated by the solver versus the experiment across the 7 sections of [Figure 15a](#).

As input, we use a mesh of a delta wing with planar faces and 800,000 metric complexity. The input mesh has 1,439,310 vertices and 8,470,523 tetrahedra while the target metric has a complexity (as defined by (A4)) of 1,600,000. The difference in complexity causes the mesh size to double during adaptation. The experiments were performed on the *wahab* cluster of Old Dominion University using dual-socket nodes equipped with two Intel<sup>®</sup> Xeon<sup>®</sup> Gold 6148 CPU @ 2.40GHz (20 slots) and 368 GB of memory. The compiler is gcc 7.5.0 and the compiler flags `-O3 -DNDEBUG -march=native`. Each run was repeated 5 times and the results were averaged using the geometrical mean [77]. For the base case, we ran the parallel code using one core.

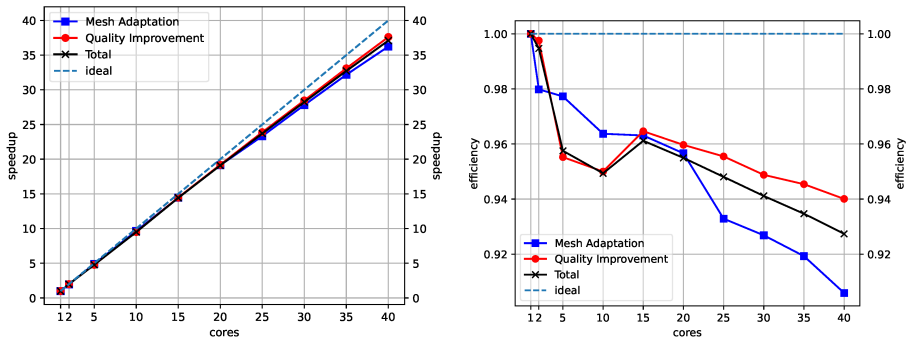


**Fig. 16:** Speedup and efficiency of the two main modules of *CDT3D* (see also Figure 1).

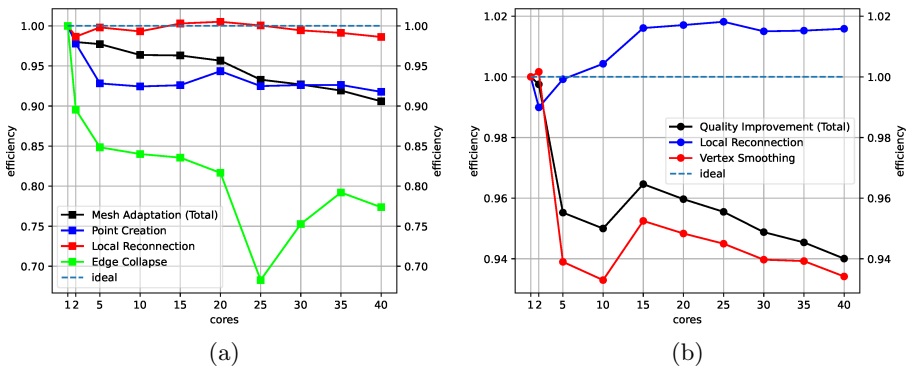


**Fig. 17:** Efficiency breakdown of the mesh adaptation and quality improvement modules of *CDT3D* (see also Figure 1).

Figure 16 depicts the total efficiency of the method as well as its breakdown with respect to the two main modules of *CDT3D* (see also Figure 1). The

end-to-end efficiency is 92.3% at 40 cores. The efficiency of the *Mesh Adaptation* and *Mesh Quality Improvement* modules are 90.5% and 94% respectively. Figure 17a presents a breakdown of the efficiency of the *Mesh Adaptation* module. The *Local Reconnection* operation performs the best with more than 98% efficiency. The super-linear speedup is caused by the “buckets”. Splitting the list of active elements into buckets and repeatedly performing reconnection over the same bucket improves the cache locality. *Point Creation* benefits from the same construct but its spin-lock implementation for updating the internal list of the contained element (see subsection 3.2) results in a lower efficiency. *Edge Collapse* exhibits a lower speedup in comparison to the other two operations due to the generic OpenMP implementation that was used to exploit parallelism. Still, this implementation of *Edge Collapse* delivers 80 – 85% efficiency for up to 20 cores and 75 – 80% efficiency for more cores. At 25 cores the edge collapse efficiency drops significantly. This is in part attributed to the dual-socket nature of the host machine. At 25 cores the code uses one and a half sockets and the OpenMP back-end of the operation does not have any special treatment for accessing memory from a different socket. For *Quality improvement* (see Figure 17b) the super-linear performance of *Local Reconnection* is more prominent due to the (approximately) constant size of the mesh during the *Quality Improvement* phase (no vertices are introduced). The *Vertex Smoothing* operation exhibits 93.4% efficiency on 40 threads. Notice also that the efficiency curve of the *Quality Improvement* stage (black) follows the trends of the smoothing operation. This is due to the fact that smoothing is the dominant operation in terms of time and also because the efficiency of *Local Reconnection* is approximately constant. Figure B8 presents a breakdown of the mesh adaptation module of *CDT3D*. *Local Reconnection* accounts for more than 75% of the total mesh adaptation time. The other two major parallel mesh operations *Point Creation* and *Edge Collapse*, are responsible for less than 10% of the mesh adaptation time. The effect of the sequential point insertion is becoming increasingly higher as expected by Amdahl’s law [78] but still, it is less than 4% of the total time.

Figure B9 depicts the percentage of the total time that corresponds to each operation. The time to smooth the vertices corresponds to about 60% of the total running time while, *Mesh Adaptation* takes about 12% of the total time.

## 6 Conclusion

In this work, we introduced a new parallel metric-based mesh adaptation method that can serve as the parallel optimistic mesh adaptation module of the *Telescopic Approach* in the context of CFD simulations. In particular, we extended the *CDT3D* library by adding new parallel mesh operations, incorporating metric adaptivity (Section 3) and the ability to interface with a CAD kernel (Section 4). The combination of these methods along with the simultaneous adaptation of surface and volume improve the quality of the mesh (as

measured by element-based measures) by 3 orders of magnitude (see Figure 5) over our initial attempt [52] that used external software for surface adaptation.

These improvements are not implemented in the void by just adding new capabilities in the mesh generation toolkit. Instead, they allow us to put the adapted meshes into use and verify that are really suitable for a class of simulations. To verify our implementation and its capability to function as a component of an adaptive pipeline - a crucial part of many real-world applications - in Sections 5.2-5.5 we tested *CDT3D* through a series of cases of increasing difficulty.

Section 5.2 served as a verification test leaving the solver outside the setup. The results match the theoretical expected values and other state-of-the-art mesh adaptation software. The solver is then introduced back in the adaptive pipeline in section 5.3 where the evaluated quantities are within less than 0.55% of the reference values in the cited literature. At the same time, Table 1 indicates that the mesh adaptation stage of our adaptive pipeline takes only a small fraction of the total core-hours required by the simulation. In section 5.4 we increased the complexity of the problem by adding a curved geometry model based on one of the most cited CFD cases. The results closely matched the experimental data as well as the ones obtained by using the solver with a carefully crafted structured mesh which is often treated as the best-case scenario in terms of mesh quality. Our last test case in the section 5.5 increased the difficulty once more by utilizing a well-known complex simulation configuration. Although our numerical results were not as close as the other cases (mainly due to the lower fidelity inviscid configuration we used), *CDT3D* was able to handle the fairly complicated CAD data in combination with the solution-based metric.

Finally, the data of section 5.6 indicate that *CDT3D* still follows a *scalability-first* [9] approach offering a well-optimized implementation attaining more than 92% end-to-end efficiency on a single node.

## 7 Future work

In this work we presented a software that uses shared memory as a basis to create a building block for scalable parallel mesh generation and adaptivity. A promising path toward extracting concurrency of mesh adaptation methods on HPC systems, the *Telescopic Approach* (see Figure 18) was proposed in [79]. The *Telescopic Approach* handles the software and hardware complexity by defining different work decomposition methods at each level of the memory hierarchy. Each method is designed to exploit the concurrency at multiple levels in parallel and adaptive simulations. However, there are some more challenges to overcome [80] and outside the scope of this paper. The next layer is the Parallel Data Refinement layer which has been already implemented with both Delaunay-based [81, 82] and Advancing-front based methods [83]. The potential scalability of these approaches were hindered by challenges related to

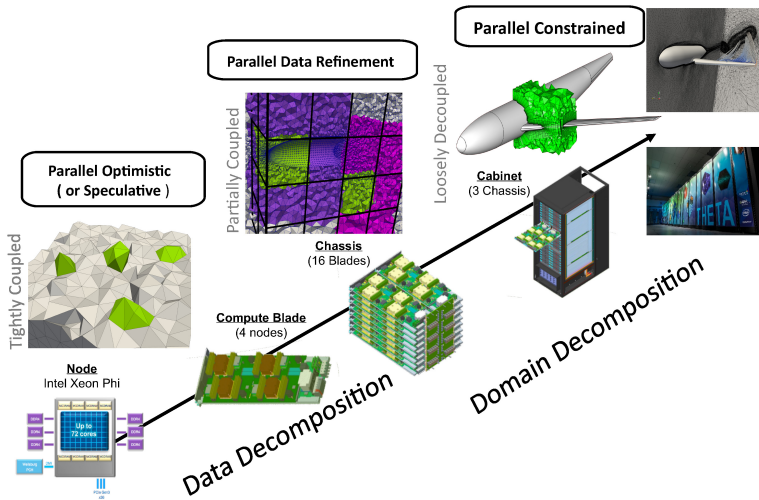


Fig. 18: The Telescopic Approach [79].

minimizing the amount of data movement as identified by [84, 82] and reducing the effect of the constrained faces on the final mesh quality as discussed in [85]. An alternative approach would be to revisit the distributed speculative approach presented in [13] and adapt it for *CDT3D*. This approach would benefit from the asynchronous message passing, automatic work-load balancing, and migration (based on data dependencies) capabilities provided by the runtime system, PREMA 2.0[86, 87] which is designed to support the Telescopic Approach.

The vertex smoothing operation can be further improved by incorporating a more complete search space for the optimal node position such as the methods presented in [50, 51]. Moreover, it could be extended to all vertices and not just the ones attached to low-quality elements providing an overall smoothed result which may provide better convergence rates for the solver. Also, CAD information such as local curvature and local feature size could be incorporated in order to optimize the quality of curved surfaces.

GPUs (Graphic Processing Units) are common in today's supercomputers however, currently, *CDT3D* make no use of them. Extending the presented meshing operations so that they can take advantage of the accelerators is expected to improve the running speed of certain operations significantly. Figure 17 reveals that almost 95% of the total time is spent on just two operations: the local reconnection and the vertex smoothing operation. Although they both exhibit more than 90% efficiency, they can still be improved by the use of accelerators. In particular, porting the inner floating-point-heavy kernels such as the predicates of the Delaunay criterion and the min-max edge-weight measure to GPUs could potentially reduce the running time significantly. We believe that such an implementation will benefit significantly from heterogeneous runtime systems like the one presented in [88] since they

allow for separating the concerns of mesh adaptation and efficient execution on accelerators reducing thus the problem complexity significantly.

As mentioned in subsections 5.4 and 5.5 we didn't succeed in obtaining viscous results with our pipeline. This is in part attributed to the absence of boundary layer mesh that many numerical methods expect. Although fully unstructured results have been reported with other solvers (see for example [89]), to the best of our knowledge, SU2 has not been tested thoroughly within this context. The boundary layer can be provided as an external procedure and integrated similarly to our work in [37]. A similar approach that combines state-of-the-art boundary layer generation with an adaptive anisotropic method appears in [90]. Another path to explore is the generation of metric-aligned meshes such as the ones presented in [43, 46]. Moreover, the use of specialized metrics may also be suitable. For example, in [91] the authors report success by combining wall-distance to their metric creation while in [92] the authors review various output-based metric construction schemes that could be evaluated.

## Acknowledgments

This research was sponsored in part by the NASA Transformational Tools and Technologies Project (NNX15AU39A) of the Transformative Aeronautics Concepts Program under the Aeronautics Research Mission Directorate, NSF grant no. CCF-1439079, the Richard T. Cheng Endowment, the Modeling and Simulation Fellowship of Old Dominion University, and the Dominion scholar fellowship of Old Dominion University. The authors would like to thank Fotis Drakopoulos for the initial implementation of the parallel vertex creation operation and the insightful discussions. Mike Park and Charles Hyde for feedback on an earlier draft of this document, Jayant Mukhopadhaya for his directions on how to configure SU2 efficiently for the delta-wing case and Kevin Garner for his insights regarding the upcoming challenges regarding the future use of *CDT3D* in a distributed memory environment.

## Appendix A Metric Spaces in the context of Mesh Adaptation

Mesh adaptation modifies an existing mesh so that it can accurately and efficiently (i.e. fewer number of elements) capture features of both the solution and the underlying domain. One of the earliest methods of mesh adaptation appears in [93] where the authors create overset meshes of different resolutions that are driven by estimates of the local truncation error. Other approaches refine or regenerate a mesh based on the magnitude and the direction of the error, utilizing an advancing front method [94] and in [95] via a Delaunay-based method. The common goal of all these approaches is to extract information about the error of the numerical solution and communicate it to the mesh adaptation method.

In this work, we adopt the *unit mesh* approach [58] where the error of the numerical solution is communicated via metric tensors. This method transforms the problem of creating the *best mesh* to creating a *unit mesh* (i.e. all edge lengths equal to 1) in a transformed space. The transformation is built such that a unit element in the transformed space reduces the error of the numerical solution back in the physical space. In practice, the method is applied by incorporating metric tensors in various geometric quantities that are used to drive decisions during mesh adaptation while staying in the physical space.

A metric tensor in three dimensions corresponds to a  $3 \times 3$  symmetric positive definite matrix  $\mathcal{M}$ <sup>15</sup>. Metric tensors in 3 dimensions can be visualized using ellipsoids. For example, the identity matrix corresponds to the unit sphere, while the matrix  $M = \begin{bmatrix} 2 & 0 & 0 \\ 0 & 1 & 0 \\ 0 & 0 & 1 \end{bmatrix}$  can be represented by an ellipsoid aligned to the coordinate axes with axes lengths 1/2, 1 and 1. For a detailed derivation of this correspondence see [11].

Using as a starting point the fact that a positive definite matrix induces an inner product through  $\langle u, v \rangle_{\mathcal{M}} := u^T \mathcal{M} v$ , one can use  $\langle u, v \rangle_{\mathcal{M}}$  to redefine how common geometric quantities are measured. For example:

$$\text{length of a segment} \quad \ell_{\mathcal{M}}(x, y) = \sqrt{\langle x - y, x - y \rangle_{\mathcal{M}}} \quad (\text{A1})$$

$$\text{angle between non-zero vectors} \quad \cos(\theta_{\mathcal{M}}) = \frac{\langle u, v \rangle_{\mathcal{M}}}{\|u\|_{\mathcal{M}} \|v\|_{\mathcal{M}}}, \quad \theta_{\mathcal{M}} \in [0, \pi] \quad (\text{A2})$$

Reference [96] presents a thorough introduction to the properties of metric tensor fields and their relation to the interpolation error of the discretized solution.

In the context of mesh adaptation, the error metric  $\mathcal{M}$  will vary from point to point and so there is a need for a way to calculate the above quantities at any point of the domain. Following the widely used approach, the Log-Euclidean framework introduced in [2] is used as interpolation scheme which can be formulated as follows: Given  $x_i, i = 1 \dots k$  be a set of vertices and  $\mathcal{M}_i = (\mathcal{M}(x_i))$  their corresponding metrics, then for a point  $x$  of the domain with barycentric coordinates  $a_i, x = \sum_{i=1}^k a_i \cdot x_i$ , with  $\sum_{i=1}^k a_i = 1$  the interpolated metric is defined by:

$$\mathcal{M}(x) = \mathcal{M}_{mean}(x) = \exp \left( \sum_{i=1}^k a_i \ln \mathcal{M}_i \right) \quad (\text{A3})$$

Note that since  $\mathcal{M}_i$  is positive definite, it has positive eigenvalues and therefore the exponential and logarithm of the metric are well defined and given by

---

<sup>15</sup>A real symmetric  $n \times n$  matrix is called *positive definite* if  $v^T M v > 0, \forall v \neq 0$

$\ln(\mathcal{M}) := P \ln(D)P^T$ ,  $\exp(\mathcal{M}) := P \exp(D)P^T$ . Where  $\mathcal{M} = PDP^T$  is the spectral decomposition of  $\mathcal{M}$ . The complexity of a discrete metric  $M$  over a mesh with  $n$  vertices is given by

$$C(M) = \sum_{i=1}^n \sqrt{\det M_i} V_i, \quad (\text{A4})$$

where  $V_i$  is the volume of the Voronoi dual element surrounding each node.

Finally, the quality measures used to report mesh quality also need to be adapted. In this work, we adopt the mesh quality measures used by the Unstructured Grid Adaptation Working Group<sup>16</sup>. The edge lengths are evaluated using:

$$L_e = \begin{cases} \frac{L_a - L_b}{\log(L_a/L_b)} & \|L_a - L_b\| > 0.001 \\ \frac{L_a + L_b}{2} & \text{otherwise} \end{cases}, \quad (\text{A5})$$

$$L_a = (v_e^T M_a v_e)^{\frac{1}{2}}, \quad L_b = (v_e^T M_b v_e)^{\frac{1}{2}}$$

where  $v_e$  is the vector along edge  $ab$ . Since the goal is to create a unit mesh, edges of length below or above 1 are considered sub-optimal. The Mean Ratio shape measure is also approximated in the discrete metric,

$$Q_K = \frac{36}{3^{1/3}} \frac{\left(|K| \sqrt{\det(M_{\text{mean}})}\right)^{\frac{2}{3}}}{\sum_{e \in L} v_e^T M_{\text{mean}} v_e}, \quad (\text{A6})$$

where  $v_e$  is the vector along the edge  $e$  of element  $K$ ,  $|K|$  the isotropic volume of the element and  $M_{\text{mean}}$  is the interpolated metric tensor evaluated at the centroid of element  $K$ . The measure is normalized by the volume of an equilateral element and as such its range is  $[0, 1]$  with 1 being the optimal quality for an element. As described in detail in [96], the first criterion is directly related to the goal of the *unit mesh* approach, which is to produce edges of length one in the transformed space. Using this criterion alone however is not enough, since it can lead to elements of volume equal or near to zero. The existence of these elements can create numerical issues in the mesh generation process which operates in finite precision and it can also cause numerical stability issues to the solver that processes the generated mesh. Combining the edge length measure with the mean ratio shape measure which achieves 1 for equilateral elements and approaches zero as the volume of the element (in the transformed space) approaches zero allows to avoid nearly flat elements.

Having established a way to communicate between the numerical solution and the mesh adaptation software it remains to specify how the error metric  $\mathcal{M}$  is evaluated. There are a number of different methods including but

<sup>16</sup><https://ugawg.github.io/> Retrieved 2023-03-30

not limited to the multiscale metric [97], output-based metrics [92], and optimization schemes [98]. For this work, the multiscale error metric is selected due to its wide use, simplicity, and availability in open-source projects like the *refine* adaptation mechanics [28]. This approach has been confirmed both theoretically [96] and experimentally [99] in a number of applications.

## Appendix B Supplementary figures

---

**Function** GenerateCandidatePoints(*t*)

---

**Input:** An active tetrahedron *t*

**Result:** Candidate point(s) for element *t*

*candidatePoints* = {}

*c* ← *centroid*(*t*)

**for** *boundary face f of t* **do**

**if** *c encroaches upon f* **then**

**if** *all edges of f are long* **then**

*p* ← *centroid*(*f*)

**for** *ridge edge e of f* **do**

                | *candidatePoints.append*(*midpoint*(*e*))

**end for**

**if** *candidatePoints is empty* **then** // no ridge was found

                | *candidatePoints.append*(*p*)

**end if**

**else**

**for** *long edge e of f* **do**

                | *candidatePoints.append*(*midpoint*(*e*))

**end for**

**end if**

**else**

        | *candidatePoints.append*(*c*)

**end if**

**end for**

**if** *candidatePoints is empty* **then**

    /\* empty means that either there are no boundary faces or no  
    encroachment occurs. In either case we keep the original point.

    \*/

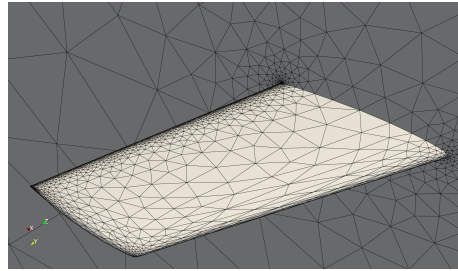
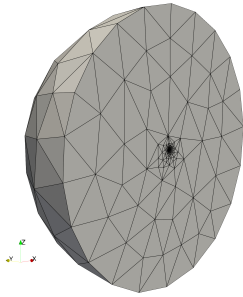
*candidatePoints.append*(*c*)

**end if**

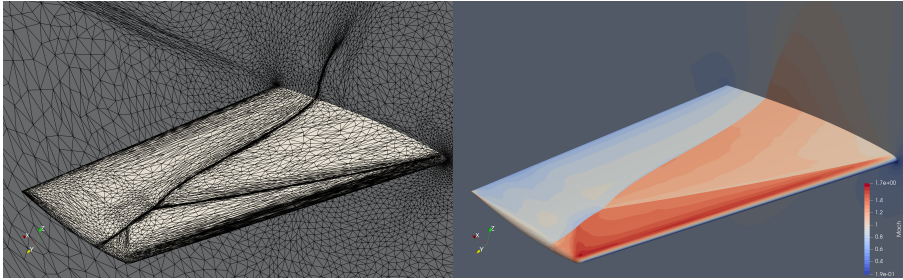
**return** *candidatePoints*

---

**Fig. B1:** Encroachment rules of the centroid-based point-creation method.



(a) Initial mesh generated by `ref bootstrap`. The mesh conforms to the geometrical features of the wing.



(b) Final iteration of the adaptive loop.

**Fig. B2:** First and last mesh of the adaptation pipeline.

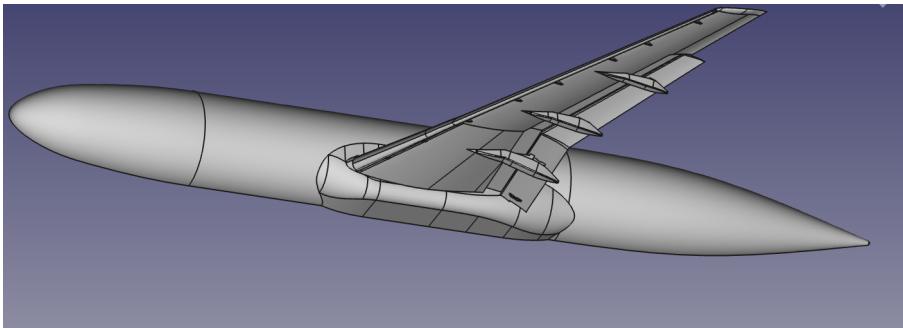


**Fig. B3:** The JSM geometry.

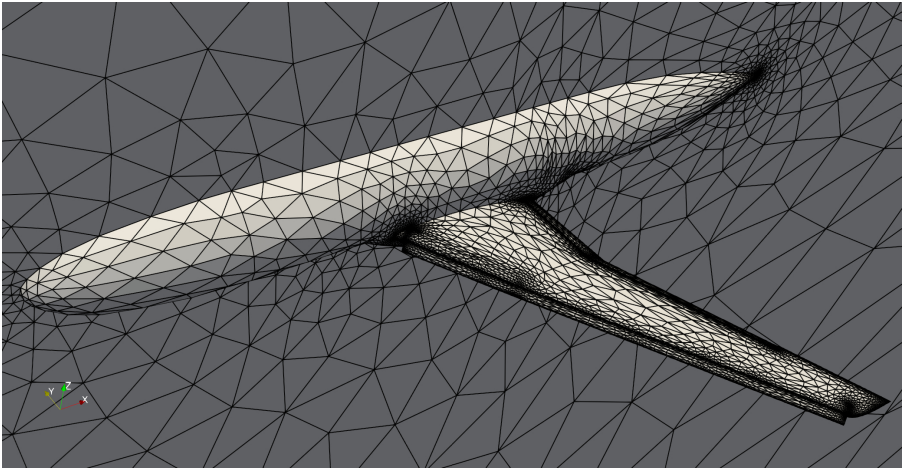


**Fig. B4:** Initial coarse mesh created by `ref bootstrap`. # vertices 52,265, # triangles 57,240, # tetrahedra : 219,230.

**Fig. B5:** Geometry and Initial mesh of the JSM case.

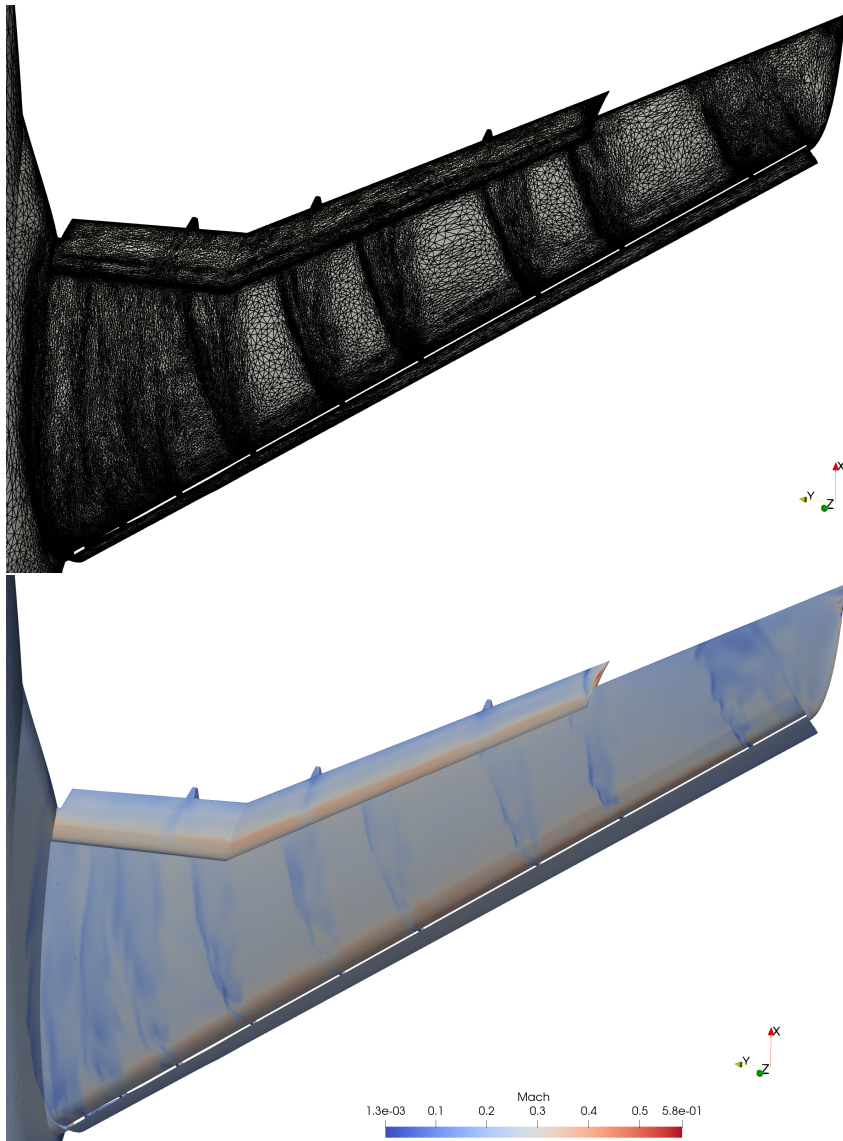


**Fig. B6:** Final mesh and coloring of the wing by the local Mach number for the JSM case.

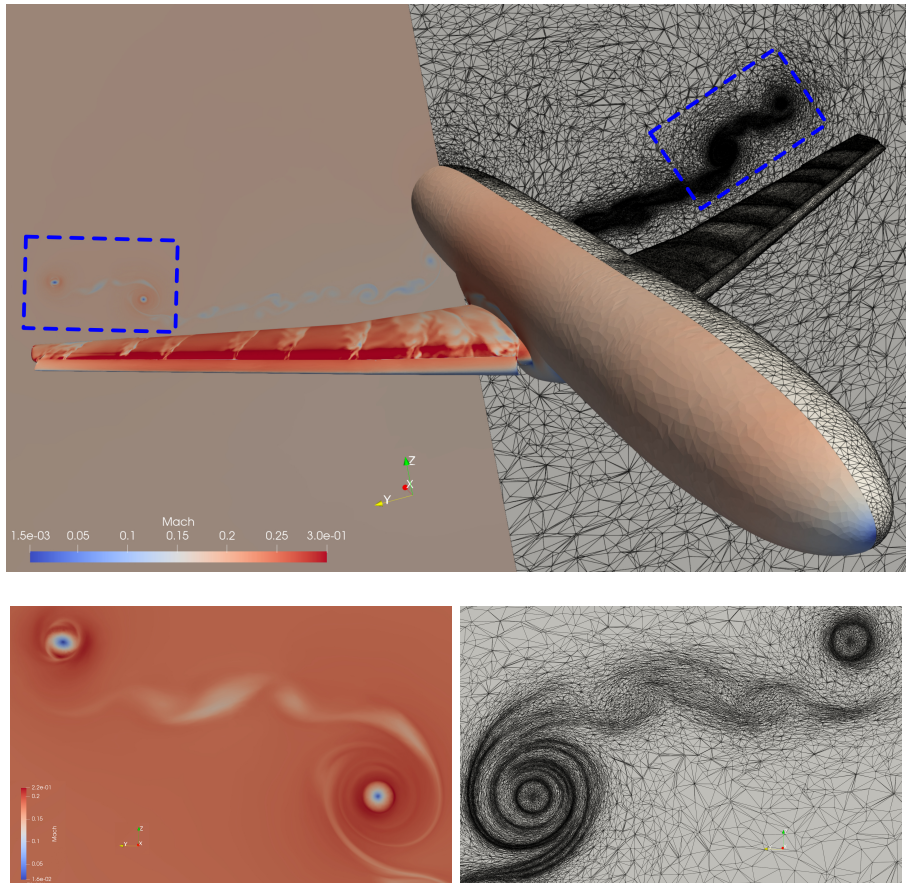


**Fig. B7:** Simulation results. Top: Final mesh alongside the corresponding solution. Bottom: Zoom-in on the blue regions of the top figure.

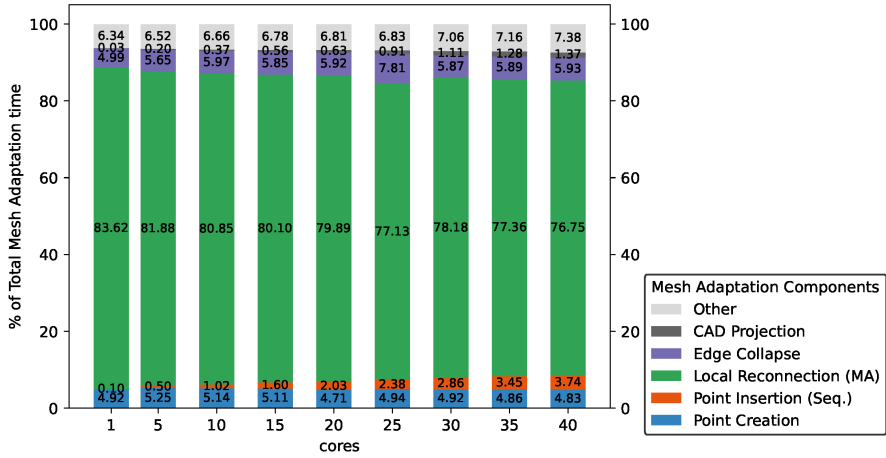


**Fig. B8:** Breakdown of the *Mesh Adaptation* time into the basic operations of *CDT3D* (see also Figure 1).

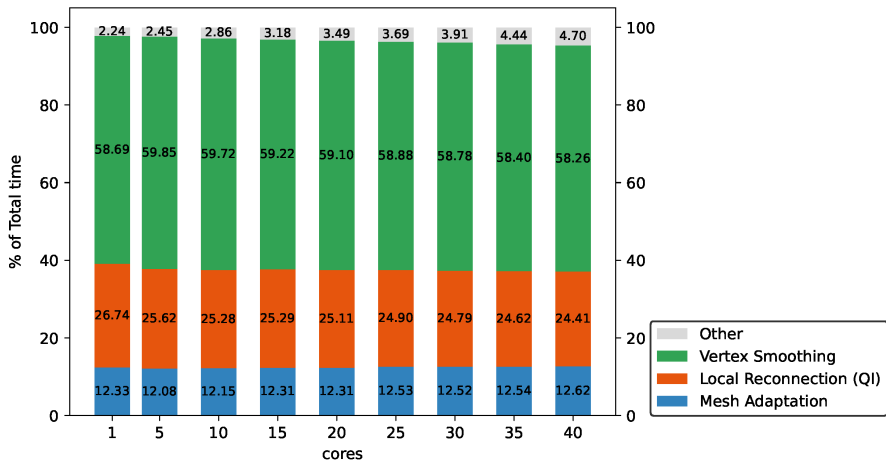


**Fig. B9:** Breakdown of the total time of *CDT3D* (see also Figure 1).

## References

- [1] M. A. Goffin, C. M. J. Baker, A. G. Buchan, C. C. Pain, M. D. Eaton, and P. N. Smith, “Minimising the error in eigenvalue calculations involving the Boltzmann transport equation using goal-based adaptivity on unstructured meshes,” *Journal of Computational Physics*, vol. 242, pp. 726–752, June 2013.
- [2] V. Arsigny, P. Fillard, X. Pennec, and N. Ayache, “Log-Euclidean metrics for fast and simple calculus on diffusion tensors,” *Magnetic Resonance in Medicine*, vol. 56, pp. 411–421, Aug. 2006.
- [3] K. Ejlebjerg Jensen, “Anisotropic Mesh Adaptation and Topology Optimization in Three Dimensions,” *Journal of Mechanical Design*, vol. 138, Apr. 2016.
- [4] A. Loseille, A. Dervieux, P. Frey, and F. Alauzet, “Achievement of Global Second Order Mesh Convergence for Discontinuous Flows with Adapted Unstructured Meshes,” in *18th AIAA Computational Fluid Dynamics Conference*, Fluid Dynamics and Co-located Conferences, American Institute of Aeronautics and Astronautics, June 2007.
- [5] T. R. Michal, D. S. Kamenetskiy, and J. Krakos, “Anisotropic Adaptive Mesh Results for the Third High Lift Prediction Workshop (HiLiftPW-3),” in *2018 AIAA Aerospace Sciences Meeting*, American Institute of Aeronautics and Astronautics, 2018.
- [6] J. Slotnick, A. Khodadoust, J. Alonso, D. Darmofal, W. Gropp, E. Lurie, and D. Mavriplis, “CFD Vision 2030 Study: A Path to Revolutionary Computational Aerosciences,” Technical Report CR-2014-218178, NASA Langley Research Center, Hampton, VA, United States, Mar. 2014.
- [7] M. A. Park, A. Loseille, J. Krakos, T. R. Michal, and J. J. Alonso, “Unstructured Grid Adaptation: Status, Potential Impacts, and Recommended Investments Towards CFD 2030,” in *46th AIAA Fluid Dynamics Conference*, American Institute of Aeronautics and Astronautics, 2016.
- [8] Oak Ridge National Lab, “Frontier supercomputer debuts as world’s fastest, breaking exascale barrier | ORNL.” <https://www.ornl.gov/news/frontier-supercomputer-debuts-worlds-fastest-breaking-exascale-barrier>, May 2022.
- [9] C. Tsolakis, N. Chrisochoides, M. A. Park, A. Loseille, and T. R. Michal, “Parallel Anisotropic Unstructured Grid Adaptation,” *AIAA Journal*, vol. 59, p. 4764–4776, Jan. 2021.
- [10] N. Chrisochoides, *Numerical Solution of Partial Differential Equations on Parallel Computers*, vol. 51 of *Lecture Notes in Computational Science and Engineering*, ch. Parallel Mesh Generation, pp. 237–264. Springer-Verlag, 2006.
- [11] C. Tsolakis, *A Unified Framework For Parallel Anisotropic Mesh Adaptation*. PhD thesis, Computer Science, Old Dominion University, Virginia, Aug. 2021.
- [12] N. Chrisochoides and D. Nave, “Parallel Delaunay mesh generation kernel,” *International Journal for Numerical Methods in Engineering*, vol. 58,

- pp. 161–176, Sept. 2003.
- [13] D. Nave, N. Chrisochoides, and L. P. Chew, “Guaranteed-quality parallel Delaunay refinement for restricted polyhedral domains,” *Computational Geometry*, vol. 28, pp. 191–215, June 2004.
  - [14] A. Bowyer, “Computing dirichlet tessellations,” *The Computer Journal*, vol. 24, pp. 162–166, jan 1981.
  - [15] D. F. Watson, “Computing the n-dimensional delaunay tessellation with application to voronoi polytopes,” *The Computer Journal*, vol. 24, pp. 167–172, jan 1981.
  - [16] P. Foteinos and N. Chrisochoides, “Dynamic Parallel 3d Delaunay Triangulation,” in *Proceedings of the 20th International Meshing Roundtable* (W. R. Quadros, ed.), pp. 3–20, Springer Berlin Heidelberg, 2011.
  - [17] P. A. Foteinos and N. P. Chrisochoides, “High quality real-time Image-to-Mesh conversion for finite element simulations,” *Journal of Parallel and Distributed Computing*, vol. 74, pp. 2123–2140, Feb. 2014.
  - [18] D. Feng, A. N. Chernikov, and N. P. Chrisochoides, “Two-level locality-aware parallel delaunay image-to-mesh conversion,” *Parallel Computing*, vol. 59, pp. 60–70, 2016.
  - [19] G. J. Gorman, G. Rokos, J. Southern, and P. H. J. Kelly, “Thread-Parallel Anisotropic Mesh Adaptation,” in *New Challenges in Grid Generation and Adaptivity for Scientific Computing*, SEMA SIMAI Springer Series, pp. 113–137, Springer, Cham, 2015.
  - [20] G. J. Gorman, “pragmatic github site.” <https://meshadaptation.github.io>, 2019.
  - [21] Dan Ibanez and Mark Shephard, “Mesh adaptation for moving objects on shared memory hardware,” in *25th International Meshing Roundtable*, 2016. Research Note.
  - [22] D. A. Ibanez, E. S. Seol, C. W. Smith, and M. S. Shephard, “PUMI: Parallel Unstructured Mesh Infrastructure,” *ACM Trans. Math. Softw.*, vol. 42, pp. 17:1–17:28, May 2016.
  - [23] H. L. de Cougny and M. S. Shephard, “Parallel volume meshing using face removals and hierarchical repartitioning,” *Computer Methods in Applied Mechanics and Engineering*, vol. 174, pp. 275–298, May 1999.
  - [24] F. Alauzet, X. Li, E. S. Seol, and M. S. Shephard, “Parallel anisotropic 3d mesh adaptation by mesh modification,” *Engineering with Computers*, vol. 21, pp. 247–258, May 2006.
  - [25] E. S. Seol and M. S. Shephard, “Efficient distributed mesh data structure for parallel automated adaptive analysis,” *Engineering with Computers*, vol. 22, pp. 197–213, Dec. 2006.
  - [26] O. Sahni, A. Ovcharenko, K. C. Chitale, K. E. Jansen, and M. S. Shephard, “Parallel anisotropic mesh adaptation with boundary layers for automated viscous flow simulations,” *Engineering with Computers*, vol. 33, pp. 767–795, Oct. 2017.
  - [27] M. Park and D. Darmofal, “Parallel Anisotropic Tetrahedral Adaptation,” in *46th AIAA Aerospace Sciences Meeting and Exhibit*, American Institute

- of Aeronautics and Astronautics, 2008.
- [28] M. A. Park, “refine : grid adaptation framework.” <https://github.com/nasa/refine>. accessed January 7, 2021.
- [29] T. Michal and J. Krakos, “Anisotropic Mesh Adaptation Through Edge Primitive Operations,” in *50th AIAA Aerospace Sciences Meeting Including the New Horizons Forum and Aerospace Exposition*, American Institute of Aeronautics and Astronautics, 2012.
- [30] A. Loseille, F. Alauzet, and V. Menier, “Unique cavity-based operator and hierarchical domain partitioning for fast parallel generation of anisotropic meshes,” *Computer-Aided Design*, vol. 85, pp. 53–67, Apr. 2017.
- [31] P. C. Caplan, “Parallel four-dimensional anisotropic mesh adaptation,” in *Proceedings of the 2022 SIAM International Meshing Roundtable*, 2022.
- [32] P. C. Caplan, “An easy way to access files in Gamma Mesh Format, the libMeshb library.” <https://gitlab.com/philipclaud/avro>, 2022.
- [33] H. Dignonnet, T. Coupez, P. Laure, and L. Silva, “Massively parallel anisotropic mesh adaptation,” *The International Journal of High Performance Computing Applications*, vol. 33, pp. 3–24, Jan. 2019. Publisher: SAGE Publications Ltd STM.
- [34] P. C. Caplan, R. Haimes, D. L. Darmofal, and M. C. Galbraith, “Four-dimensional anisotropic mesh adaptation,” *Computer-Aided Design*, vol. 129, p. 102915, 2020.
- [35] F. Drakopoulos, *Finite Element Modeling Driven by Health Care and Aerospace Applications*. PhD thesis, Computer Science, Old Dominion University, Virginia, July 2017.
- [36] F. Drakopoulos, C. Tsolakis, and N. P. Chrisochoides, “Fine-Grained Speculative Topological Transformation Scheme for Local Reconnection Methods,” *AIAA Journal*, vol. 57, pp. 4007–4018, July 2019.
- [37] B. Y. Zhou, B. Diskin, N. R. Gauger, J. K. Pardue, A. Chernikov, C. Tsolakis, F. Drakopoulos, and N. P. Chrisochoides, “Hybrid RANS/LES Simulation of Vortex Breakdown Over a Delta Wing,” in *AIAA Aviation 2019 Forum*, AIAA AVIATION Forum, (Dallas, Texas), American Institute of Aeronautics and Astronautics, June 2019.
- [38] C. L. Lawson, “Software for C1 Surface Interpolation,” in *Mathematical Software* (J. R. Rice, ed.), pp. 161–194, Academic Press, Jan. 1977.
- [39] H. Borouchaki, P. L. George, F. Hecht, P. Laug, and E. Saltel, “Delaunay mesh generation governed by metric specifications. Part I. Algorithms,” *Finite Elements in Analysis and Design*, vol. 25, pp. 61–83, Mar. 1997.
- [40] C. Dobrzynski and P. Frey, “Anisotropic Delaunay Mesh Adaptation for Unsteady Simulations,” in *Proceedings of the 17th International Meshing Roundtable* (R. V. Garimella, ed.), pp. 177–194, Springer Berlin Heidelberg, 2009.
- [41] T. J. Barth, “Numerical aspects of computing high Reynolds number flows on unstructured meshes,” in *29th Aerospace Sciences Meeting*, American Institute of Aeronautics and Astronautics, 1991.
- [42] D. L. Marcum and F. Alauzet, “Unstructured Mesh Generation Using

- Advancing Layers and Metric-Based Transition for Viscous Flowfields,” in *21st AIAA Computational Fluid Dynamics Conference*, American Institute of Aeronautics and Astronautics, 2013.
- [43] A. Loseille, “Metric-orthogonal Anisotropic Mesh Generation,” *Procedia Engineering*, vol. 82, pp. 403–415, Jan. 2014.
- [44] A. Chernikov, C. Antonopoulos, N. Chrisochoides, S. Schneider, and D. Nikolopoulos, “Experience with Memory Allocators for Parallel Mesh Generation on Multicore Architectures,” in *International Conference on Numerical Grid Generation in Computational Field Simulations*, (Forth, Crete, Greece), Sept. 2007.
- [45] J. R. Shewchuk, “Tetrahedral Mesh Generation by Delaunay Refinement,” in *Proceedings of the Fourteenth Annual Symposium on Computational Geometry*, SCG ’98, (New York, NY, USA), pp. 86–95, ACM, 1998.
- [46] D. Marcum and F. Alauzet, “Aligned Metric-based Anisotropic Solution Adaptive Mesh Generation,” *Procedia Engineering*, vol. 82, pp. 428–444, 2014.
- [47] C. Tsolakis, P. Thomadakis, and N. Chrisochoides, “Tasking framework for adaptive speculative parallel mesh generation,” *The Journal of Supercomputing*, vol. 78, pp. 1–32, October 2021.
- [48] W. R. Buell and B. A. Bush, “Mesh Generation - A Survey,” *Journal of Engineering for Industry*, vol. 95, pp. 332–338, Feb. 1973.
- [49] D. Ibanez, N. Barral, J. Krakos, A. Loseille, T. Michal, and M. Park, “First benchmark of the Unstructured Grid Adaptation Working Group,” *Procedia Engineering*, vol. 203, pp. 154–166, Jan. 2017.
- [50] L. A. Freitag and C. Ollivier-Gooch, “Tetrahedral mesh improvement using swapping and smoothing,” *International Journal for Numerical Methods in Engineering*, vol. 40, pp. 3979–4002, Nov. 1997.
- [51] B. M. Klingner, *Improving tetrahedral meshes*. Ph.D., University of California, Berkeley, United States – California, 2008.
- [52] C. Tsolakis, N. Chrisochoides, M. A. Park, A. Loseille, and T. R. Michal, “Parallel Anisotropic Unstructured Grid Adaptation,” in *AIAA Scitech 2019 Forum*, AIAA SciTech Forum, (San Diego, California), American Institute of Aeronautics and Astronautics, Jan. 2019.
- [53] N. J. Taylor and R. Haines, “Geometry Modelling: Underlying Concepts and Requirements for Computational Simulation (Invited),” in *2018 Fluid Dynamics Conference*, American Institute of Aeronautics and Astronautics, 2018.
- [54] R. Haines and J. Dannenhoffer, “The Engineering Sketch Pad: A Solid-Modeling, Feature-Based, Web-Enabled System for Building Parametric Geometry,” in *21st AIAA Computational Fluid Dynamics Conference*, American Institute of Aeronautics and Astronautics, 2013.
- [55] M. A. Park, W. L. Kleb, W. T. Jones, J. A. Krakos, T. R. Michal, A. Loseille, R. Haines, and J. Dannenhoffer, “Geometry Modeling for Unstructured Mesh Adaptation,” in *AIAA Aviation 2019 Forum*, AIAA AVIATION Forum, American Institute of Aeronautics and Astronautics, June 2019.

- [56] M. A. Park, “refine : grid adaptation framework.” <https://github.com/nasa/refine>.
- [57] R. Haimes and M. Drela, “On The Construction of Aircraft Conceptual Geometry for High-Fidelity Analysis and Design,” in *50th AIAA Aerospace Sciences Meeting including the New Horizons Forum and Aerospace Exposition*, Aerospace Sciences Meetings, American Institute of Aeronautics and Astronautics, Jan. 2012.
- [58] F. Alauzet, “Size gradation control of anisotropic meshes,” *Finite Elements in Analysis and Design*, vol. 46, pp. 181–202, Jan. 2010.
- [59] T. D. Economou, F. Palacios, S. R. Copeland, T. W. Lukaczyk, and J. J. Alonso, “SU2: An Open-Source Suite for Multiphysics Simulation and Design,” *AIAA Journal*, vol. 54, no. 3, pp. 828–846, 2016.
- [60] M. O’Connell, C. Druryor, K. B. Thompson, K. Jacobson, W. K. Anderson, E. J. Nielsen, J.-R. Carlson, M. A. Park, W. T. Jones, R. Biedron, E. M. Lee-Rausch, and B. Kleb, “Application of the Dependency Inversion Principle to Multidisciplinary Software Development,” in *2018 Fluid Dynamics Conference*, American Institute of Aeronautics and Astronautics, June 2018.
- [61] H. Si, “TetGen, a Delaunay-Based Quality Tetrahedral Mesh Generator,” *ACM Transactions on Mathematical Software*, vol. 41, no. 2, pp. 11:1–11:36, 2015.
- [62] D. L. Marcum and N. P. Weatherill, “Unstructured grid generation using iterative point insertion and local reconnection,” *AIAA Journal*, vol. 33, no. 9, pp. 1619–1625, 1995.
- [63] L. Maréchal, “An easy way to access files in Gamma Mesh Format, the libMeshb library.” <https://github.com/LoicMarechal/libMeshb>, 2021.
- [64] Y. Bourgault, M. Picasso, F. Alauzet, and A. Loseille, “On the use of anisotropic a posteriori error estimators for the adaptative solution of 3D inviscid compressible flows,” *International Journal for Numerical Methods in Fluids*, vol. 59, no. 1, pp. 47–74, 2009.
- [65] W. G. Habashi, J. Dompierre, Y. Bourgault, D. Ait-Ali-Yahia, M. Fortin, and M.-G. Vallet, “Anisotropic mesh adaptation: towards user-independent, mesh-independent and solver-independent CFD. Part I: general principles,” *International Journal for Numerical Methods in Fluids*, vol. 32, no. 6, pp. 725–744, 2000.
- [66] M. C. Galbraith, P. C. Caplan, H. A. Carson, M. A. Park, A. Balan, W. K. Anderson, T. Michal, J. A. Krakos, D. S. Kamenetskiy, A. Loseille, F. Alauzet, L. Frazza, and N. Barral, “Verification of Unstructured Grid Adaptation Components,” *AIAA Journal*, vol. 58, no. 9, pp. 3947–3962, 2020.
- [67] Z. J. Wang, K. Fidkowski, R. Abgrall, F. Bassi, D. Caraeni, A. Cary, H. Deconinck, R. Hartmann, K. Hillewaert, H. T. Huynh, N. Kroll, G. May, P.-O. Persson, B. v. Leer, and M. Visbal, “High-order CFD methods: current status and perspective,” *International Journal for Numerical Methods in Fluids*, vol. 72, no. 8, pp. 811–845, 2013.

- [68] T. Leicht and R. Hartmann, “Error estimation and anisotropic mesh refinement for 3d laminar aerodynamic flow simulations,” *Journal of Computational Physics*, vol. 229, pp. 7344–7360, Sept. 2010.
- [69] A. Balan, M. A. Park, S. Wood, and W. K. Anderson, “Verification of Anisotropic Mesh Adaptation for Complex Aerospace Applications,” in *AIAA Scitech 2020 Forum*, AIAA SciTech Forum, American Institute of Aeronautics and Astronautics, Jan. 2020.
- [70] R. Hartmann, J. Held, T. Leicht, and F. Prill, “Error Estimation and Adaptive Mesh Refinement for Aerodynamic Flows,” in *ADIGMA - A European Initiative on the Development of Adaptive Higher-Order Variational Methods for Aerospace Applications* (N. Kroll, H. Bieler, H. Deconinck, V. Couaillier, H. van der Ven, and K. Sørensen, eds.), Notes on Numerical Fluid Mechanics and Multidisciplinary Design, (Berlin, Heidelberg), pp. 339–353, Springer, 2010.
- [71] V. Schmitt and F. Charpin, “Pressure Distributions on the ONERA-M6-Wing at Transonic Mach Numbers,” in *Experimental Data Base for Computer Program Assessment: Report of the Fluid Dynamics Panel Working Group 04*, pp. B1:1–B1:44, NATO Research and Technology Organisation AGARD, May 1979.
- [72] H. Nishikawa and B. Diskin, “Customized Grid Generation Codes for Benchmark Three-Dimensional Flows,” in *2018 AIAA Aerospace Sciences Meeting*, AIAA SciTech Forum, American Institute of Aeronautics and Astronautics, Jan. 2018.
- [73] T. Ito, Y. Yokokawa, H. Ura, H. Kato, K. Mitsuo, and K. Yamamoto, “High-Lift Device Testing in JAXA 6.5M X 5.5M Low-Speed Wind Tunnel,” in *25th AIAA Aerodynamic Measurement Technology and Ground Testing Conference*, Fluid Dynamics and Co-located Conferences, American Institute of Aeronautics and Astronautics, June 2006.
- [74] Y. Yokokawa, M. Murayama, M. Kanazaki, K. Murota, T. Ito, and K. Yamamoto, “Investigation and Improvement of High-Lift Aerodynamic Performances in Low-speed Wind Tunnel Testing,” in *46th AIAA Aerospace Sciences Meeting and Exhibit*, Aerospace Sciences Meetings, American Institute of Aeronautics and Astronautics, Jan. 2008.
- [75] Y. Yokokawa, M. Murayama, H. Uchida, K. Tanaka, T. Ito, K. Yamamoto, and K. Yamamoto, “Aerodynamic Influence of a Half-Span Model Installation for High-Lift Configuration Experiment,” in *48th AIAA Aerospace Sciences Meeting Including the New Horizons Forum and Aerospace Exposition*, Aerospace Sciences Meetings, American Institute of Aeronautics and Astronautics, Jan. 2010.
- [76] C. L. Rumsey, J. P. Slotnick, and A. J. Scafani, “Overview and Summary of the Third AIAA High Lift Prediction Workshop,” *Journal of Aircraft*, vol. 56, pp. 621–644, Dec. 2018. Publisher: American Institute of Aeronautics and Astronautics.
- [77] P. J. Fleming and J. J. Wallace, “How not to lie with statistics: the correct way to summarize benchmark results,” *Communications of the*

- ACM*, vol. 29, pp. 218–221, Mar. 1986.
- [78] G. M. Amdahl, “Validity of the single processor approach to achieving large scale computing capabilities,” in *Proceedings of the April 18-20, 1967, Spring Joint Computer Conference*, AFIPS ’67 (Spring), (New York, NY, USA), pp. 483–485, ACM, 1967.
- [79] N. P. Chrisochoides, “Telescopic Approach for Extreme-Scale Parallel Mesh Generation for CFD Applications,” in *46th AIAA Fluid Dynamics Conference*, American Institute of Aeronautics and Astronautics, 2016.
- [80] K. Garner, C. Tsolakis, P. Thomadakis, and N. Chrisochoides, “Towards distributed speculative adaptive anisotropic parallel mesh generation,” in *AIAA Aviation 2024 Forum*, AIAA AVIATION Forum, American Institute of Aeronautics and Astronautics, 2024. submitted.
- [81] D. Feng, C. Tsolakis, A. N. Chernikov, and N. P. Chrisochoides, “Scalable 3D Hybrid Parallel Delaunay Image-to-mesh Conversion Algorithm for Distributed Shared Memory Architectures,” *Comput. Aided Des.*, vol. 85, pp. 10–19, Apr. 2017.
- [82] P. Thomadakis and N. Chrisochoides, “Experience with distributed memory delaunay-based image-to-mesh conversion implementation,” 2023. arXiv:2308.12525 [cs.DC].
- [83] K. M. Garner, P. Thomadakis, T. Kennedy, C. Tsolakis, and N. N. Chrisochoides, “On the End-User Productivity of a Pseudo-Constrained Parallel Data Refinement Method for the Advancing Front Local Reconnection Mesh Generation Software,” in *AIAA Aviation 2019 Forum*, American Institute of Aeronautics and Astronautics, June 2019.
- [84] D. Feng, A. N. Chernikov, and N. P. Chrisochoides, “A hybrid parallel Delaunay image-to-mesh conversion algorithm scalable on distributed-memory clusters,” *Computer-Aided Design*, vol. 103, pp. 34–46, Oct. 2018.
- [85] K. Garner, “Parallelization of the Advancing Front Local Reconnection Mesh Generation Software Using a Pseudo-Constrained Parallel Data Refinement Method,” Master’s thesis, Computer Science, Old Dominion University, 2020.
- [86] P. Thomadakis, C. Tsolakis, and N. Chrisochoides, “Multithreaded runtime framework for parallel and adaptive applications,” *Engineering with Computers*, vol. 38, p. 4675–4695, July 2022.
- [87] P. Thomadakis and N. Chrisochoides, “Toward runtime support for unstructured and dynamic exascale-era applications,” *The Journal of Supercomputing*, vol. 79, p. 9245–9272, Jan. 2023.
- [88] P. Thomadakis and N. Chrisochoides, “Runtime support for performance portability on heterogeneous distributed platforms,” 2023. arXiv:2303.02543 [cs.DC].
- [89] M. A. Park, N. Barral, D. Ibanez, D. S. Kamenetskiy, J. A. Krakos, T. R. Michal, and A. Loseille, “Unstructured Grid Adaptation and Solver Technology for Turbulent Flows,” in *2018 AIAA Aerospace Sciences Meeting*, American Institute of Aeronautics and Astronautics, 2018.

- [90] D. L. Marcum and F. Alauzet, “Unstructured Mesh Generation Using Advancing Layers and Metric-Based Transition for Viscous Flowfields,” in *21st AIAA Computational Fluid Dynamics Conference*, American Institute of Aeronautics and Astronautics, 2013.
- [91] H. Sukas and M. Sahin, “HEMLAB Algorithm Applied to the High-Lift JAXA Standard Model,” in *AIAA Scitech 2021 Forum*, American Institute of Aeronautics and Astronautics, 2021.
- [92] K. J. Fidkowski and D. L. Darmofal, “Review of Output-Based Error Estimation and Mesh Adaptation in Computational Fluid Dynamics,” *AIAA Journal*, vol. 49, no. 4, pp. 673–694, 2011.
- [93] M. J. Berger and J. Olinger, “Adaptive mesh refinement for hyperbolic partial differential equations,” *Journal of Computational Physics*, vol. 53, pp. 484–512, Mar. 1984.
- [94] J. Peraire, M. Vahdati, K. Morgan, and O. C. Zienkiewicz, “Adaptive remeshing for compressible flow computations,” *Journal of Computational Physics*, vol. 72, pp. 449–466, Oct. 1987.
- [95] D. J. Mavriplis, “Adaptive mesh generation for viscous flows using triangulation,” *Journal of Computational Physics*, vol. 90, pp. 271–291, Oct. 1990.
- [96] A. Loseille and F. Alauzet, “Continuous Mesh Framework Part I: Well-Posed Continuous Interpolation Error,” *SIAM Journal on Numerical Analysis*, vol. 49, no. 1, pp. 38–60, 2011.
- [97] F. Alauzet and A. Loseille, “High-order sonic boom modeling based on adaptive methods,” *Journal of Computational Physics*, vol. 229, pp. 561–593, Feb. 2010.
- [98] M. Yano and D. L. Darmofal, “An optimization-based framework for anisotropic simplex mesh adaptation,” *Journal of Computational Physics*, vol. 231, pp. 7626–7649, Sept. 2012.
- [99] A. Loseille and F. Alauzet, “Continuous Mesh Framework Part II: Validations and Applications,” *SIAM Journal on Numerical Analysis*, vol. 49, pp. 61–86, Jan. 2011.